Comparison of Acoustic Radiation Force Impulse (ARFI) Imaging and Shear Wave Imaging (SWI) in Evaluation of Myocardial Ablation Lesions

by

Lily Kuo

Department of Biomedical Engineering
Duke University

Date:_____

Approved:

_____
Gregg Trahey, Supervisor

_____
Patrick Wolf

_____
Jeremy Dahl

Thesis submitted in partial fulfillment of
the requirements for the degree of
Master of Science in the Department of
Biomedical Engineering in the Graduate School
of Duke University

2013

ABSTRACT

Comparison of Acoustic Radiation Force Impulse (ARFI) Imaging and Shear Wave Imaging (SWI) in Evaluation of Myocardial Ablation Lesions

by

Lily Kuo

Department of Biomedical Engineering
Duke University

Date:_____

Approved:

_____
Gregg Trahey, Supervisor

_____
Patrick Wolf

_____
Jeremy Dahl

An abstract of a thesis submitted in partial fulfillment of the requirements for the degree of Master of Science in the Department of Biomedical Engineering in the Graduate School of Duke University

2013

Abstract

Radiofrequency ablation (RFA) is commonly used to treat cardiac arrhythmias, by generating a series of discrete RFA lesions in the myocardium to isolate arrhythmogenic conduction pathways. The size of each lesion is controlled by the temperature of the tissue at the surface or the duration of RF power delivery, but feedback on the extent and transmurality of the generated lesion are unavailable with current technology. Intracardiac Echocardiography (ICE) may provide a solution through Acoustic Radiation Force Impulse (ARFI) imaging or Shear Wave Imaging (SWI), which each generate images of local mechanical compliance from very small ultrasonically-induced waves. This work compares ARFI and SWI in an ex-vivo experiment for lesion boundary assessment and lesion gap resolution.

Contents

List of Tables

List of Figures

Acknowledgements

This work was made possible by grant funding from the NIH grants R37HL096023 and R01EB01248 and Siemens Medical Systems for technical support. Work on this study could not have been possible without the unwavering support of my thesis advisor, Professor Gregg Trahey, and the graduate and undergraduate students on our research team. I would like to specifically thank Peter Hollender for his guidance and support throughout every aspect of this research, without whom this study could not have been completed, Stephanie Eyerly for her consultation during the development of the ablation and histological procedures, Patrick Wolf for his expertise in electrophysiology and ablation procedure development, and Virginia Chen for her help in the initial development of the procedural set-up.

This work could not have been possible without the loving encouragement of my family.

1. Introduction

1.1 Cardiac Arrhythmias

Intrinsically, the heart is an electrically conducting muscle which is capable of initiating its own sinus rhythm. The sinoatrial (SA) node, a tight bundle of tissue in the right atrium of the heart, behaves as an independent cardiac pacemaker. Cardiac arrhythmias arise from irregularities in cardiac function, and are characterized by abnormalities in heart rhythm and electrical conduction.

During a normal heart beat, an electrical impulse is initiated in the SA node, where the impulse travels through conducting tissue in the form of cardiac action potentials throughout the right and left atria to the atrioventricular (AV) node, located at the interatrial septum. From the AV node, the electrical impulse is transmitted down through the septum of the heart, via a bundle of highly conductive fibers known as the bundle of His. The branches extending from the bundle of His are Purkinje fibers. The electrical activity travels through the Purkinje fibers, which extend from the septum through the apex of the heart, up through the ventricular walls of the heart.[1]

These timed, electrically propagating stimuli in the heart activate the myocytes, causing different sections of myocardium to contract rhythmically. A normal sinus rhythm allows the heart to contract so that the chambers of the heart are able to pump blood through the circulatory system efficiently. As irregularities in the sinus rhythm

[1] (Dubin 2000)

arise due to pathophysiologies and anatomical defects, myocardial contraction becomes abnormal and the heart fails to function properly.

Generally, cardiac arrhythmias can be grouped into a few anatomical categories: supraventricular tacchyarrhythmias, ventricular arrhythmias, and bradyarrhythmias. [2] Tachycardias like atrial, multifocal atrial, and junctional ectopic, and ventricular tachycardia are characterized by abnormally fast heart rates with focal origins, while bradyarrhythmic events like atrioventricular block manifest in such a way that heart rate becomes abnormally slow. Atrial fibrillation and atrial flutter are arrhythmic conditions where irregularities in conduction cause uncoordinated atrial contraction, leading to inefficient pumping to the ventricles, diminishing effective circulation. The severity of an arrhythmia depends on its origin and physical manifestation; while ventricular fibrillation describes irregular and uncoordinated phenomena related to atrial fibrillation, ventricular fibrillation is a more fatal arrhythmia because ventricular failure causes circulation to halt almost entirely.

The most commonly sustained cardiac arrhythmia is atrial fibrillation (AF).[3] Often asymptomatic and undiagnosed, atrial fibrillation is caused by a number of conditions, the most prevalent being: mitral valve disease, coronary heart disease (with myocardial infarct or angina onset), congenital heart disease, Wolff-Parkinson-White

[2] (Kastor 2000)
[3] (Kastor 2000)

syndrome, rheumatic heart disease, pericarditis, and cardiomyopathy. To fully appreciate the prevalence of atrial fibrillation among patients with the above conditions, the percent of patients that develop AF for some listed conditions can be seen in Table 1.

Table 1: Patients' existing cardiac conditions with atrial fibrillation (AF).[4]

Existing condition	AF occurrence (%)
Mitral valve stenosis	40-50%
Myocardial infarction	11%
Congenital heart disease	20%
Wolff-Parkinson-White syndrome	35%
Pericarditis	35-70%
Cardiomyopathy	15-25%

These structural defects and disease states prevent the myocardium from contracting properly. Though often asymptomatic, patients who have AF may present with palpitations, shortness of breath, sudden onset of stroke or transient ischemic attack. AF is often diagnosed by examination of an electrocardiogram (ECG), where the P wave may be absent, and R-R intervals are irregular overall.

The broad range of atrial fibrillation causes result in varying levels of fibrillation permanence. Paroxysmal, or sudden onset, atrial fibrillation is characterized by recurring episodes that spontaneously revert back to normal sinus rhythm. Persistent atrial fibrillation, on the other hand, can be characterized by a longer lasting (several

[4] (Kastor 2000)

days) attack that can be corrected with cardioversion therapy, which will be discussed in Section 1.2. Permanent atrial fibrillation is defined as an on-going long term (year or more) episode of fibrillation, generally untreatable by a single session of cardioversion.

1.2 Overview of Arrhythmia Treatments

1.2.1 Chemical Cardioversion

The primary method of controlling chronic AF is with pharmacological treatment. Different forms of drugs can be used to reduce ventricular rate and sustain sinus rhythm. These drugs are considered chemical cardioversion medications that can be administered orally or intravenously. The most commonly used chemical cardioversion drugs are: β-adrenergic blockers, calcium-channel blocking agents, sodium channel blockers (like quinidine), and re-polarization prolonging agents (like amiodarone). These medications help to block influences on heart rate at the AV node level, slowing atrial fibrillation to a rate closer to sinus rhythm. Pharmacological treatment can often only decrease heart rate to around 90 beats per minute; because of the rate controlling properties, accessibility, and cost of drugs, chemical cardioversion is the most commonly used form of long term AF treatment.[5] However, with its relatively low conversion success rate (average of 21 – 71% success), chemical cardioversion can result in a more costly overall treatment with dosage failures.[6]

---

[5] (Kastor 2000)
[6] (Naccarelli, et al. 2000)

1.2.2 Electrical Cardioversion

Electrical cardioversion is a conditionally effective way to convert chronic AF to normal sinus rhythm (NSR). NSR is restored in 70- 90% of patients with AF who undergo electrical cardioversion therapy.[7] Depending on the causes and circumstances surrounding the AF, electrical cardioversion provides immediate NSR conversion. In this generally hospital-administered method of treatment, two electrode pads are placed on the patient's chest – one placed right parasternally in an anterior position, and the other placed along the midaxillary line in a lateral position. Around 50 Joules of energy are delivered via defibrillator; the procedure ends with restoration of NSR, or with a few attempts at the highest level of stored energy.[8] Patients with chronic or persistent AF receive electrical cardioversion concurrent with pharmacological treatment, while patients who present with the first paroxysm of AF are not given antiarrhythmic treatment prior to electrical cardioversion. Certain patient populations respond more effectively to electrical cardioversion than others. For example, treatment works better for patients who have shorter-appearing atrial fibrillation compared to patients who have permanent AF; stenotic mitral valve disease caused AF is more susceptible to electrical cardioversion therapy than AF caused by regurgitant mitral valve diseases. In patients who have undergone cardiac surgery, electrical cardioversion is not a preferred method of cardioversion treatment.

---

[7] (Van Gelder, et al. 1991)
[8] (Van Gelder, et al. 1991)

While electrical cardioversion is highly effective at the time of delivery, arrhythmia often re-develops within 1 year of the successful cardioversion treatment. As shown in Table 2, a high percentage of patients experience a re-occurrence of AF immediately following successful electrical cardioversion therapy. Unless other therapy (pharmacological or otherwise) is introduced after cardioversion, the arrhythmia will most likely return.

Table 2: Percentage of patients experiencing re-occurrence of atrial fibrillation or other forms of cardiac arrhythmia following successful electrical cardioversion therapy[9]

Time after therapy	AF re-occurrence
< 1 Hr	90%
< 24 Hrs	70%
< 1 month	60%
< 3 months	50%
< 1 year	20 - 35%

While electrical cardioversion is safe and effective for most patients, its high re-occurrence and non-permanence are major drawbacks. Particularly for patients with permanent AF, electrical and chemical cardioversion are not sustained, effective treatments.

1.2.3 Radiofrequency Ablation

Radiofrequency ablation (RFA) is a permanent treatment used to treat the malfunctioning electrophysiology of the heart; its purpose is to block errant electrical

[9] (Kastor 2000)

conductivity in the myocardium. Lesions, which are no longer electrically conductive, are created in pre-determined locations to block unwanted electrical automaticity and specific paths of re-entrant electrical activity that cause arrhythmias. In atrial fibrillation, paths of micro-re-entry occur throughout the atria; RFA procedures for treatment of AF involve atria-localized electrical isolation around pulmonary veins. In pulmonary vein isolation procedures, linear ablation is achieved by re-positioning the ablation catheter every 15-20 seconds during ablation.[10] A typical set of lesion set in AF ablation procedures can be seen in Figure 1.

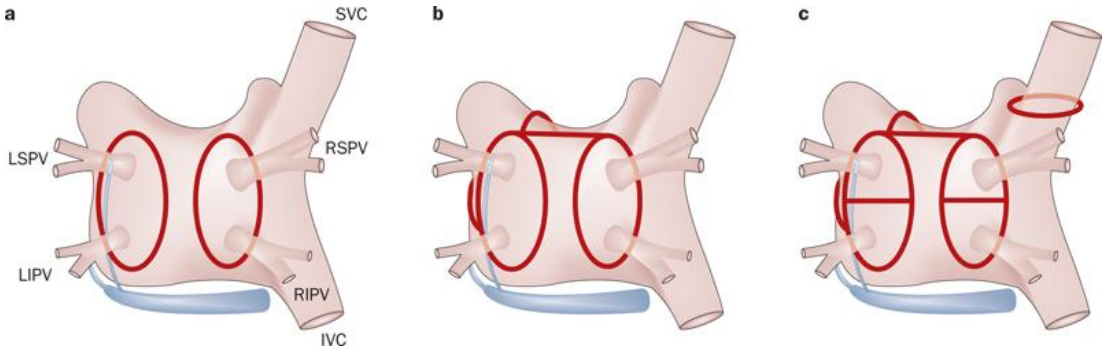

Figure 1: A schematic of common lesion sets used during atrial fibrillation RFA treatments can be seen here. The figure shows the posterior view of the atria. As can be seen, the pulmonary veins, which branch off the posterior end of the left atria on both the right and left sides. Pulmonary vein isolation uses linear ablation around the entirety of the pulmonary vein branches in each case (a, b, c), and includes an isolation of the superior vena cava, branching off the anterior right atrium. This figure is borrowed from Dewire & Calkins (2010). [11]

[10] (Wilber, Packer and Stevenson 2008)
[11] (Dewire and Calkins 2010)

RFA is performed using an ablation catheter, which delivers radiofrequency (RF) energy, with an alternating current (AC) at approximately 500 Hz delivery frequency; the mechanism through which this procedure works is via myocardial heating.[12] During a procedure, the ablation catheter is brought into contact with myocardial tissue while a skin electrode serves as electrical ground. At the blood/tissue interface where the ablation catheter tip is, there is an impedance increase and voltage drop when RF energy is applied. The tissue heating that occurs as a result causes local myocardial tissue necrosis through protein denaturation. The size of the lesion formed will depend on the temperature, power delivery, size and force of catheter tip contact, and duration of the ablation procedure.[13]

Due to the slight variations in myocardial anatomy, ablation catheter specifications, and physician procedure nuances, lesion growth and procedure complications are somewhat variable.[14] Particularly in linear ablation procedures, this variability can be highly limiting. There are significant trade-offs when optimizing lesion sizes; while small lesions would limit collateral damage, they may result in insufficient necrosis and elimination of arrhythmia. Creating large lesions could result in oversize and unwanted conduction blocks. Very high temperatures could cause blood boiling,

[12] (Wilber, Packer and Stevenson 2008)
[13] (Jain and Wolf 1999)
[14] (Ho, et al. 2007)

resulting in coagulation, or steam bubble formation, which could rupture through endocardial and epicardial surfaces.[15]

RFA procedures are guided by Intracardiac Echocardiography (ICE), fluoroscopy, and/or electroanatomical mapping (EAM). Currently, ICE is used to image the contact of the ablation catheter and the surface of the myocardium, but it is unable to show contrast of lesions for assessment following the RFA procedure.[16]

1.3 Radiofrequency Ablation Assessment

The myocardium must be assessed before and after the RFA procedure to ensure its full effectiveness. Prior to ablating, anatomical and electrical mapping is often used for successful treatment planning. Initial planning allows a physician to precisely target regions in the myocardium to effectively block the arrhythmic pathway. Because of variability among patients and procedures, RFA often results in lesions with varying sizes and shapes. After-ablation assessment is crucial in determining the effective extent of electrical conduction blocking to evaluate the procedure completeness.

1.3.1 Target Localization Electrical Mapping

Activation sequence mapping is used to visualize tachycardias with focal regions. This target localization map superimposes tissue conduction velocities onto an anatomical model so that the focal origin can be identified. Using electrogram

---

[15] (Wilber, Packer and Stevenson 2008)
[16] (Marrouche, et al. 2003)

recordings from different locations throughout the myocardium, fiducial points on the electrocardiogram (ECG) like the P wave or QRS onset are chosen. The relation between time delays in the ECGs and distance from chosen focus are used in calculating the tissue conduction velocity.[17]

Activation sequence mapping does not have high resolution sensitivity when mapping regions of anisotropic conduction. In cases of re-entrant arrhythmia, an activation sequence map shows continuous activity, where the "early" and the "late" designations are directly adjacent.

Because activation sequence mapping cannot always capture the entire tachycardic cycle length, other methods of mapping are required to accurately map re-entrant arrhythmias. Entrainment mapping charts the continuous resetting of re-entry circuits. In entrainment mapping, the pacing of the excitation is studied – excitable gaps in the circuits correspond to re-entrant pathways. Entrainment mapping is limited by stable re-entrant pathways; paroxysmal and episodic tachycardias may be difficult to characterize without continuous circuits.

Because electrical mapping measures electrical activity only on the endocardial surface, it assumes a level of homogeneous and transmural damage to the tissue. This regionally-specific limitation does not account for the complex and heterogenous characteristics that may underlie the effective extent of RFA treatment.

---

[17] (Wilber, Packer and Stevenson 2008)

1.3.2 Electroanatomical Mapping

Electroanatomical mapping (EAM) techniques provide a three-dimensional anatomic model with overlaying electrical function. Underlying anatomy is modeled by imaging with mapping systems like the BioSense Webster Carto; the electrical map is superimposed on the 3D anatomical model.

In RFA procedures, EAM systems are used to guide ablation catheter placement, catheter position tracking and annotation during ablation, and post-ablation substrate conduction mapping.[18] The major drawback of EAM following ablation is that while mapping systems provide information about intended lesion placement after treatment, EAM is unable to directly visualize the resulting lesion formation, and as such, the treated myocardium cannot be fully and accurately assessed with EAM.

Conduction block is rarely seen in lesion gaps measuring greater than 5 mm, but is variable in gaps measuring between 2-5 mm, and gap sizes as small as 0.1 mm have been found to conduct electrical activity.[19] These discontinuities created in linear ablations are unlikely to be characterized by EAM, which is unable to map electrical conductivity away from the endocardial surface, or identify electrically stunned myocardium.[20]

---

[18] (Pappone, et al. 2001)
[19] (Melby, et al. 2008)
[20] (Nademanee, et al. 2010)

1.3.3 Ultrasonic Elasticity Imaging

Ultrasonic elasticity imaging is used to visualize the differences in tissue elasticity. By mechanically exciting the tissue, tissue response can be imaged to ultrasonically visualize structures that share similar ultrasonic echogenicities, but have different mechanical properties.[21] In this way, ultrasonic elasticity imaging provides structural information that otherwise cannot be visualized in clinical ultrasound.[22]

1.3.3.1 Acoustic Radiation Force Impulse (ARFI)

ARFI imaging is a qualitative ultrasound-based technique that is used to create 2D images of relative tissue elasticity. The acoustic radiation force applied transiently deforms soft tissue; this local dynamic displacement response of the tissue can be tracked ultrasonically.[23] Relative tissue displacement measurements can be attributed to the underlying tissue compliance: assuming a simple linear, elastic model, soft tissue is more displaceable than stiff tissue.[24]

When a rapid ultrasonic pulse (10-100 μs) pulse is focused at a target region within the tissue, the energy is absorbed and tissue is briefly displaced away from the ultrasound transducer before recovering within a few milliseconds. High speed ultrasound captures the motion in the target region during displacement, and the process is repeated across a number of locations in the field of view.

---

[21] (Palmeri and Nightingale 2011)
[22] (Wells and Liang 2011)
[23] (Fahey, et al. 2005)
[24] (Nightingale, Soo, et al. 2002)

Eyerly, et al., have shown the viability of intracardiac ARFI imaging in visualizing myocardial lesions following RFA procedures.[25]

1.3.3.2 Shear Wave Imaging (SWI)

Shear wave elasticity imaging (SWEI or SWI) uses acoustic excitation similar to ARFI, but tracks the propagation of shear waves away from the transducer, created by the excitation.[26] The local group velocity of the shear wave is proportional to tissue elasticity, such that:

$$c_T = \sqrt{\mu/\rho}$$

Where: c_T is the shear wave speed [m/s], μ is the shear modulus [kPa], and ρ is the density [g/cm^2].

Assuming an elastic model with semi-infinite, incompressible, linear elastic medium, the shear wave velocity can be calculated and attributed to the quantitative shear modulus of the tissue.[27]

In shear wave speed estimation of SWI, shear wave arrival time differences can be tracked at a single location or at multiple locations. In SWI – Single-Track Location (SWI-STL), adjacent excitation locations are calculated at a single receive location; SWI – Multiple-Track Location (SWI-MTL) uses multiple adjacent receive locations to measure time differences between different shear waves. While both track methods provide a

[25] (Eyerly, et al. 2012)
[26] (Sarvazyan, et al. 1998)
[27] (Nightingale, et al. 2003)

quantitative shear wave velocity estimate, SWI-STL is similar to the spatially modulated ultrasound radiation force (SMURF) imaging method developed by McAleavey, et al (2007).[28]

[28] (McAleavey, Menon and Orszulak 2007)

2. Methodology

2.1 Beam Sequences

To create large, uniform ARFI/SWI images, the AcuNav was operated in linear mode. Excitation pulses with 6 MHz, 750-cycles were used to mechanically excite the tissue and induce ARFI displacements and shear wave propagation. Each plane wave transmit excitation was generated with a 32 element sub-aperture, measuring 3.54 mm, focused at 15 mm depth. To image the mechanical response of the excitation, 32 parallel receive lines were beamformed about the excitation, extending 2.25 mm to either side of the excitation. The data was acquired rapidly at 10,000 frames per second following the excitation for a total of 5 ms at each location, using 40% bandwidth tracking. Transmit and tracking voltage was set to 90 V. This entire sequence was electronically translated across the aperture in 16 steps, so that each excitation was spaced apart by 0.15 mm distance. This limited transducer edge effects on the excitation, while receive was captured across the full aperture.

For the clinical scan beam sequences used in the linear ablation procedure, 32 ARF transmit locations imaged a 45° field of view.

2.2 Ex-vivo Experimental Set-Up

The experimental set-up is shown in Figure 2. A custom water tank was placed on the translation stage and filled with saline solution with impedance measuring

approximately 115-130 Ω and temperature ranging between 35-37° C.

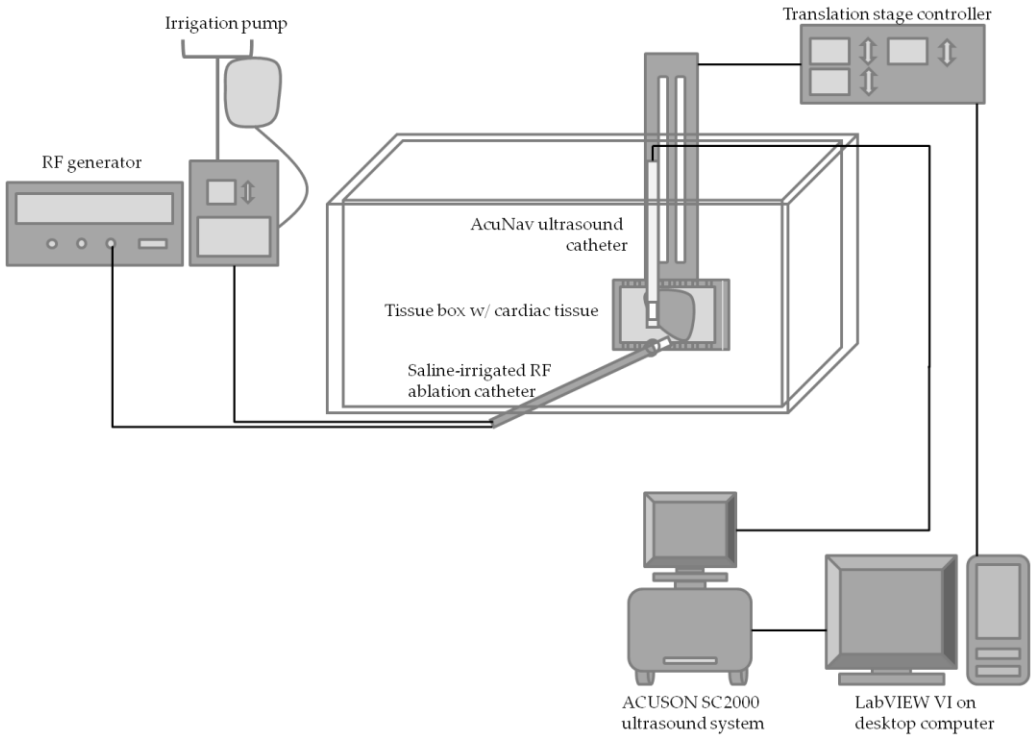

Figure 2: The entire experimental set-up is shown here. The tissue sample is mounted in a box that has been secured to the translation stage, which is remote control translated in the x, y, and z directions.

The custom tissue box containing the heart tissue sample was mounted on the translation stage and lowered into the saline filled water tank. A custom LabView VI concurrently remote controlled the translation stage and triggered ARFI/SWI data acquisition at each position in the sampling grid during imaging.

During the ablation procedure, the BioSense Webster ThermoCool irrigated tip ablation catheter was inserted through the front of the water tank to come into contact with the endocardial side of the tissue sample.

Prior to imaging and ablation, the ablation catheter and ICE imaging catheter were aligned in elevation using a point target.

2.3 Experimental Procedure

Heart samples were obtained from healthy porcine subjects. Sections of right ventricular tissue basal to the papillary muscles. The tissue sample was then degassed in a Varian DS202 Vacuum degassing chamber for 30 minutes at -25 inHg. The degassed tissue was mounted in a custom box on anechoic rubber and oriented so that visible muscle striations ran parallel to the z-direction (elevational imaging plane) of the set-up.

2.3.1 Ablation

Prior to performing the Radiofrequency Ablation (RFA) procedure, three pre-scans of the unperturbed myocardial samples were obtained as control comparison. Post-ablation imaging was performed five minutes after RF ablation to prevent discrepant imaging of conductive lesion growth immediately following ablation.

2.3.1.1 Lesion Pairs

Two radiofrequency (RF) ablation lesions were created along the center lateral line following the pre-scan. The BioSense Webster ThermoCool irrigated tip ablation catheter was manually brought into full contact with the endocardial surface of the tissue. Controlled by the BioSense Webster Stockert 70 RF generator, 22 W of power was applied for 60 seconds while the BioSense Webster CoolFlow system irrigated the catheter tip with 0.9% NaCl saline at 30 mL/min. Lesion locations were pre-determined

and distance between the centers ranged from 10 to 12 mm, limiting gap sizes between 0.5 to 3 mm.

2.3.1.2 Line of lesions

Following the ablation procedure specifications detailed in Section 2.3.1.1, lines of RFA lesions were created along the elevational imaging plane (along the basal-apical axis of the myocardium) across an entire sample of tissue. Ablation locations varied from 8 to 12 mm in distance.

2.3.2 Imaging

Using a Siemens Acuson AcuNav 10-French ICE imaging catheter and a Siemens SC2000 Ultrasound scanner, custom linear and clinical beam sequences were used in imaging the tissue. By translating the tissue laterally and elevationally, a grid of evenly spaced data was sampled and constructed into three-dimensional volumes.

Table 3: Imaging grid spacing

Configuration	Lateral extent (mm)	Lateral increments (mm)	Elevational extent (mm)	Elevational increments (mm)
Linear	28.8	2.4	14.4	0.3
Clinical (phased)	56	7	14.4	0.3

The phased array beam sequences were designed for clinical use; limitations of phased array imaging include non-uniform sampling, angular sensitivity and post-process scan conversion inaccuracies. ARFI/SWI data were acquired before and after ablation; two sets of 3D volumetric data was acquired each tissue sample.

2.4 Histological Preparation

Following post-ablation imaging, the tissue was sliced along the center axis of the ablation lesions and frozen between 5 and 12 hours. The frozen tissue was then sliced in the elevational plane with 5 and 10 mm spacing to either side of the center axis. Slice increments were chosen to optimize efficacy of the stain within the tissue; endocardial and epicardial surfaces are somewhat resistant to TTC stain.

2.4.1 TTC Stain

A standard triphenyltetrazolium chloride (TTC) staining protocol was used to visualize the contrast between the ablation lesions and the surrounding healthy tissue.

[1] The 200 mL buffer solution contained 542.4 mg of NaH_2PO_4 dissolved in 45.2 mL H_2O and 2198.15 mg of Na_2HPO_4 dissolved in 154.8 mL H_2O. 2g of TTC was added and dissolved into the buffer solution and kept at a temperature of 37°C in a water bath. The defrosted tissue slices were then put into the TTC staining solution and stirred every minute for a total of 15 minutes.

2.4.2 Cryoslicing

Immediately after staining, the tissue slices were placed in a Peel-A-Way 22 x 40 mm x 20 mm deep embedding mold and frozen in Tissue-Tek O.C.T. Compound at -20°C. After at least 5 hours of freezing time, the O.C.T. embedded tissue was sliced in the elevational plane using a Microm HM 505 E Cryptome. The tissue was

[1] (Fishbein, et al. 1981)

photographed after each 0.15 mm slice; the slicing increment size was chosen to correspond to half the elevational increments of the acquired ARFI/SWI data for comparable constructed 3D ultrasound and histology volumes.

2.5 Image Post-processing

After data acquisition, images were created during post-processing to compare the different imaging methods. Brightness-mode (B-Mode), ARFI, shear wave imaging–single track location (SWI-STL), and shear wave imaging – multiple track location (SWI-MTL) images were generated and compared.

2.5.1 Shear Wave Speed Estimation

Axial tissue displacement between successive frames was measured with a phase-root seeking algorithm. The ARFI images were formed through displacement averaging about the center 4 imaging lines through 0.2 ms after excitation.

Displacement estimates away from the center lines were used to generate shear wave estimates using arrival-time estimators. For each excitation, displacement curves were filtered with a 100 Hz to 1 kHz bandpass filter and a directional filter. The arrival time at each pixel was found using time-to-peak estimation. To calculate the shear wave velocity estimate, the reciprocal of the time difference between adjacent receive locations was used. Because the receive locations overlap from several excitation pushes, arrival time differences from times of arrival from each push excitation were averaged together; these estimates were used in SWI- Multiple-Track Location (SWI-MTL). Alternatively,

the arrival time differences at a single receive location for adjacent excitation locations were calculated and averaged across spatial locations for estimates used in SWI- Single-Track Location (SWI-STL).

3. Results

Images from the ARFI/SWI scan sequences, B-Mode acquisition, and histology were stitched together to create three-dimensional volumes and cross-sectional scans.

3.1 Ablation Lesion Imaging

Pre- and post- ablation scans were acquired for each sample to identify inherent anatomical structural anomalies and confirm ablation lesion growth. The Brightness-Mode (B-Mode), Acoustic Radiation Force Impulse (ARFI), Shear Wave Imaging – Single Track Location (SWI-STL), Shear Wave Imaging – Multiple Track Location (SWI-MTL) images were created and aligned for comparison. In the post-ablation scan set, TTC-stain (histology) images were also included to confirm the lesion sizes and gap spacing between lesions. Histology images are taken from photographs of the corresponding slice; for the cross-sectional scans, an axial plane slice corresponding to the axial depth of the ARFI/SWI generated image is stitched together. The images appear as green channel RGB data, because the lesions appear white relative to the red-stained myocardial tissue.

3.1.1 Cross-sectional Imaging Modality Comparison

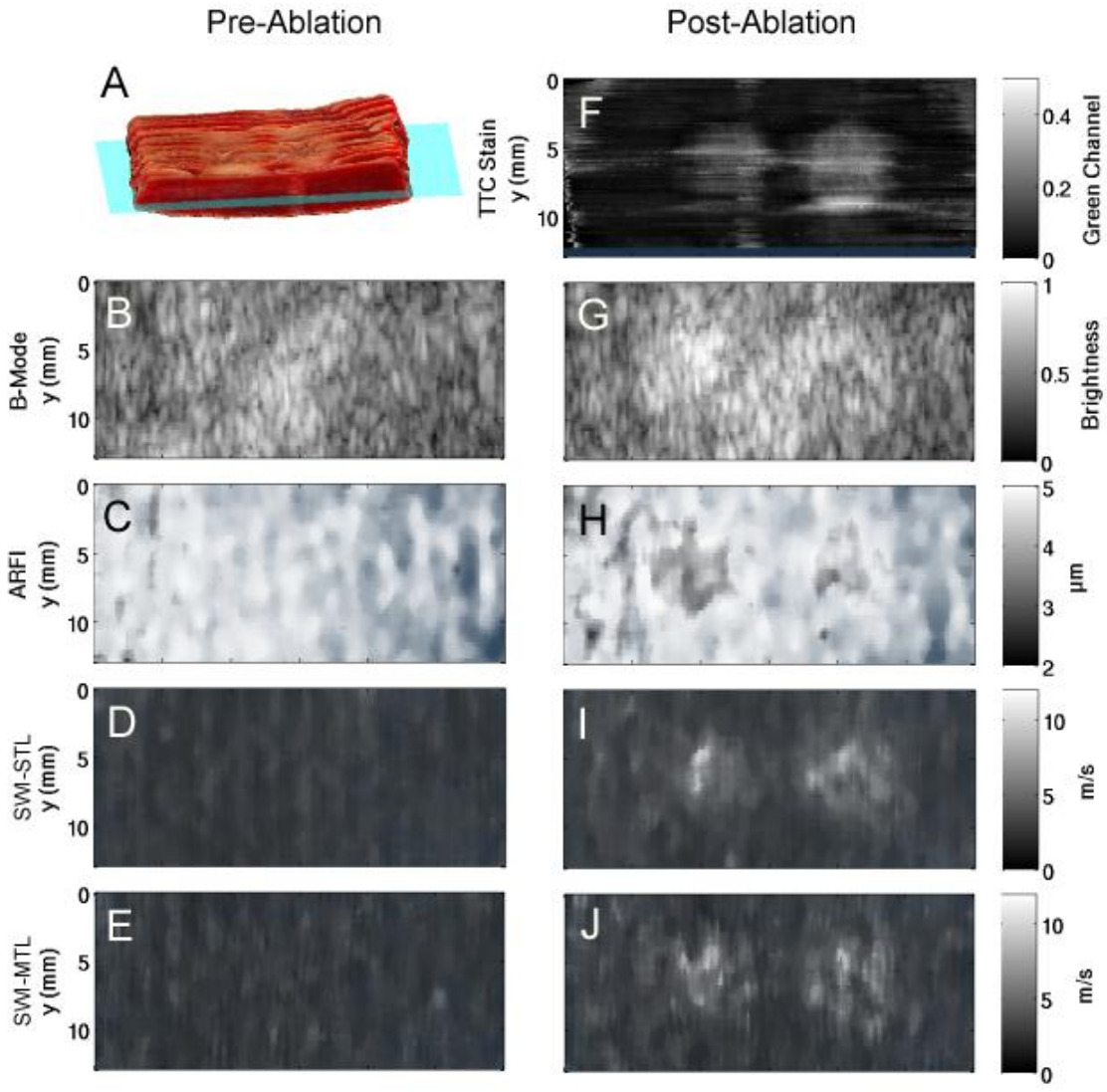

Figure 3: A comparison between all imaging modalities can be seen in this pre- and post-ablation set. (A): re-constructed TTC-stain 3D volume showing the cross-sectional area depth in relation to the volume. (B) B-Mode pre-ablation; (C) ARFI pre-ablation; (D) SWI-STL pre-ablation; (E) SWI-MTL pre-ablation; (F) TTC-stained cross-section; (G) B-Mode post-ablation; (H) ARFI post-ablation; (I) SWI-STL post-ablation; (J) SWI-MTL post-ablation

3.1.2 Cross-sectional Gap Variation Comparison

3.1.2.1 ARFI Images

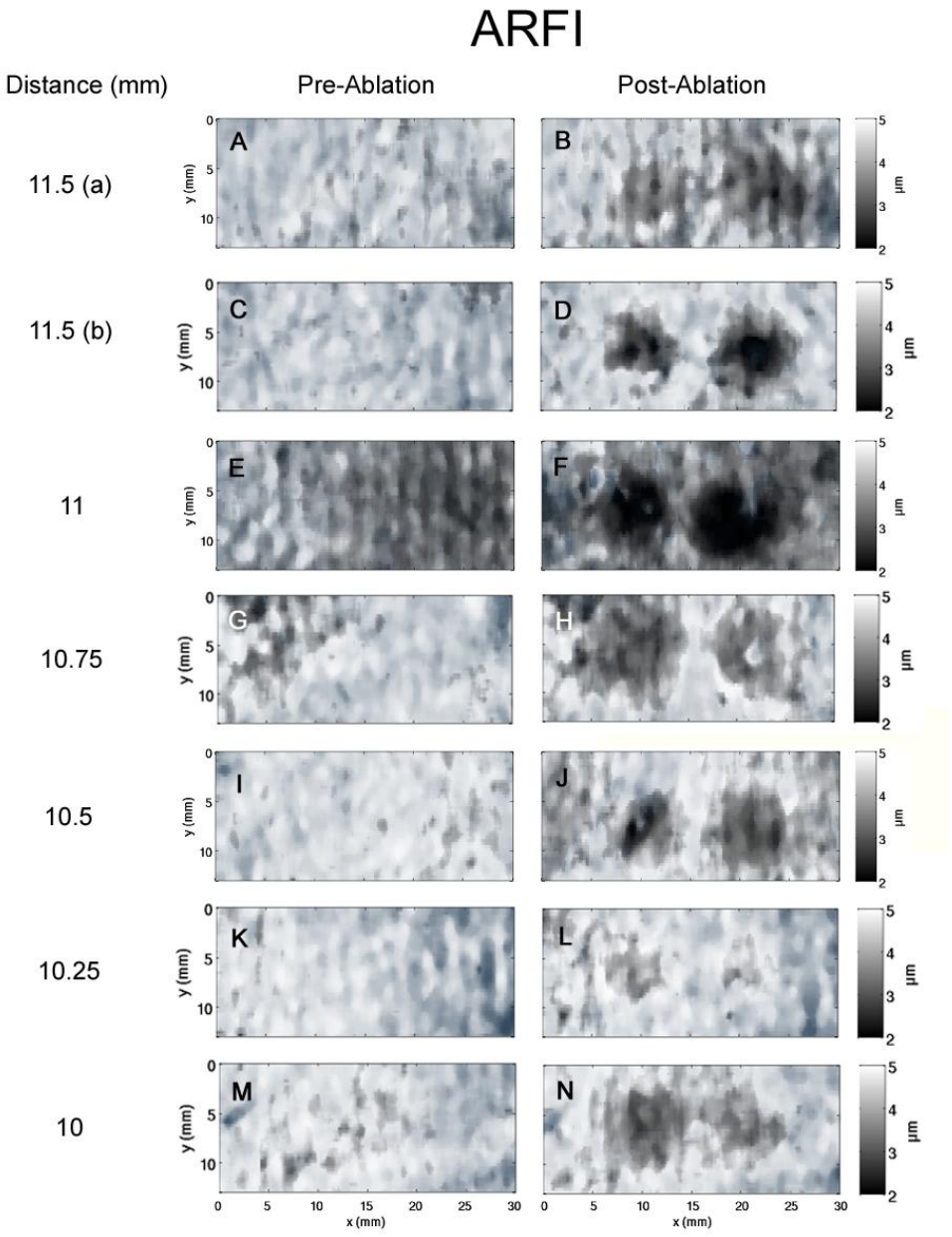

Figure 4: Cross-sectional pre- and post- ablation ARFI scans were constructed from the 3D imaging volume to compare the lesion sizes and gap spacing between different samples. Distance is measured between lesion centers. ARFI displacements are shown as dynamic ranges between 2 and 5 μm.

3.1.2.2 SWI-STL

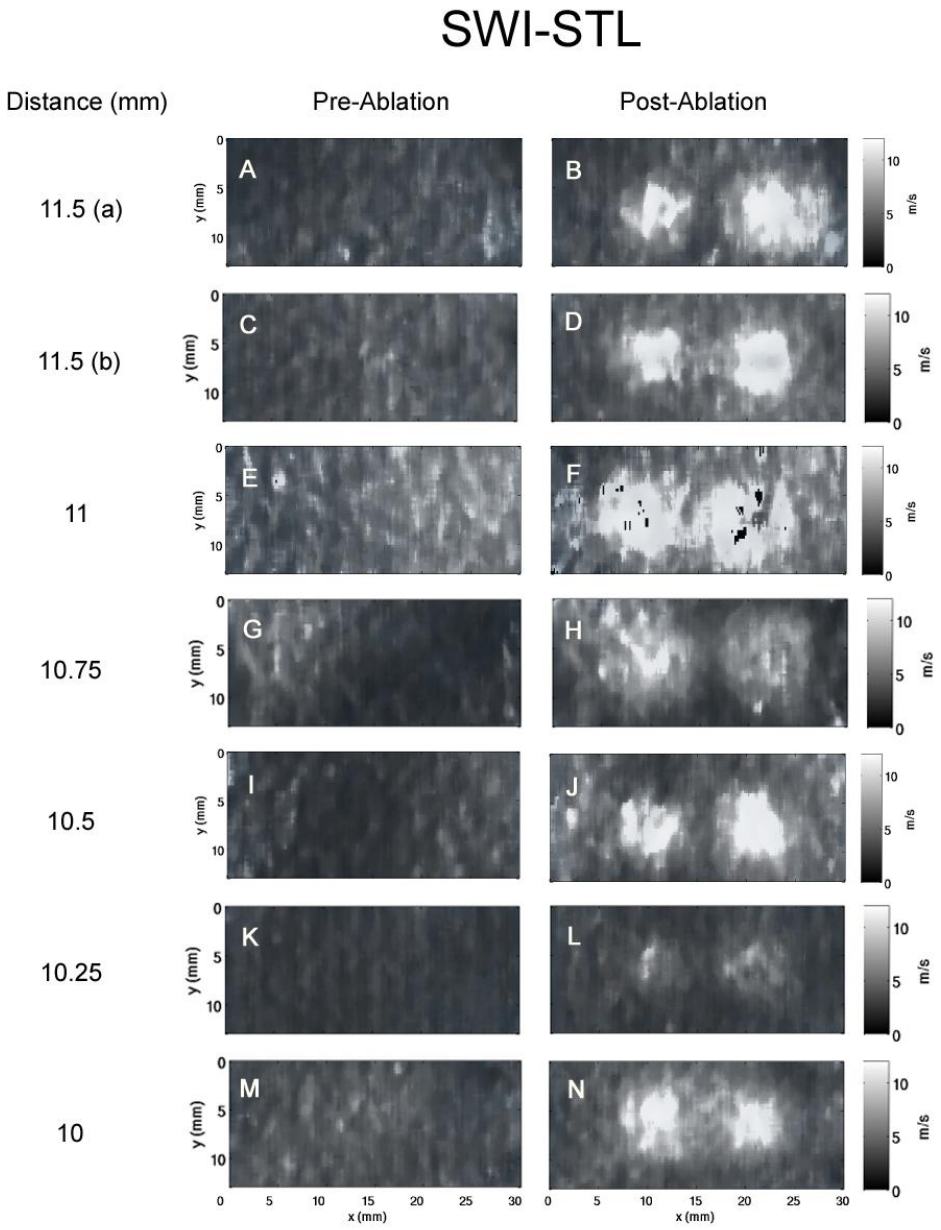

Figure 5: Cross-sectional pre- and post- ablation SWI-STL scans were constructed from the 3D imaging volume. Distance is measured between lesion centers. Shear wave velocity estimates are shown as a dynamic range between 0 and 10 m/s.

3.1.2.3 SWI-MTL

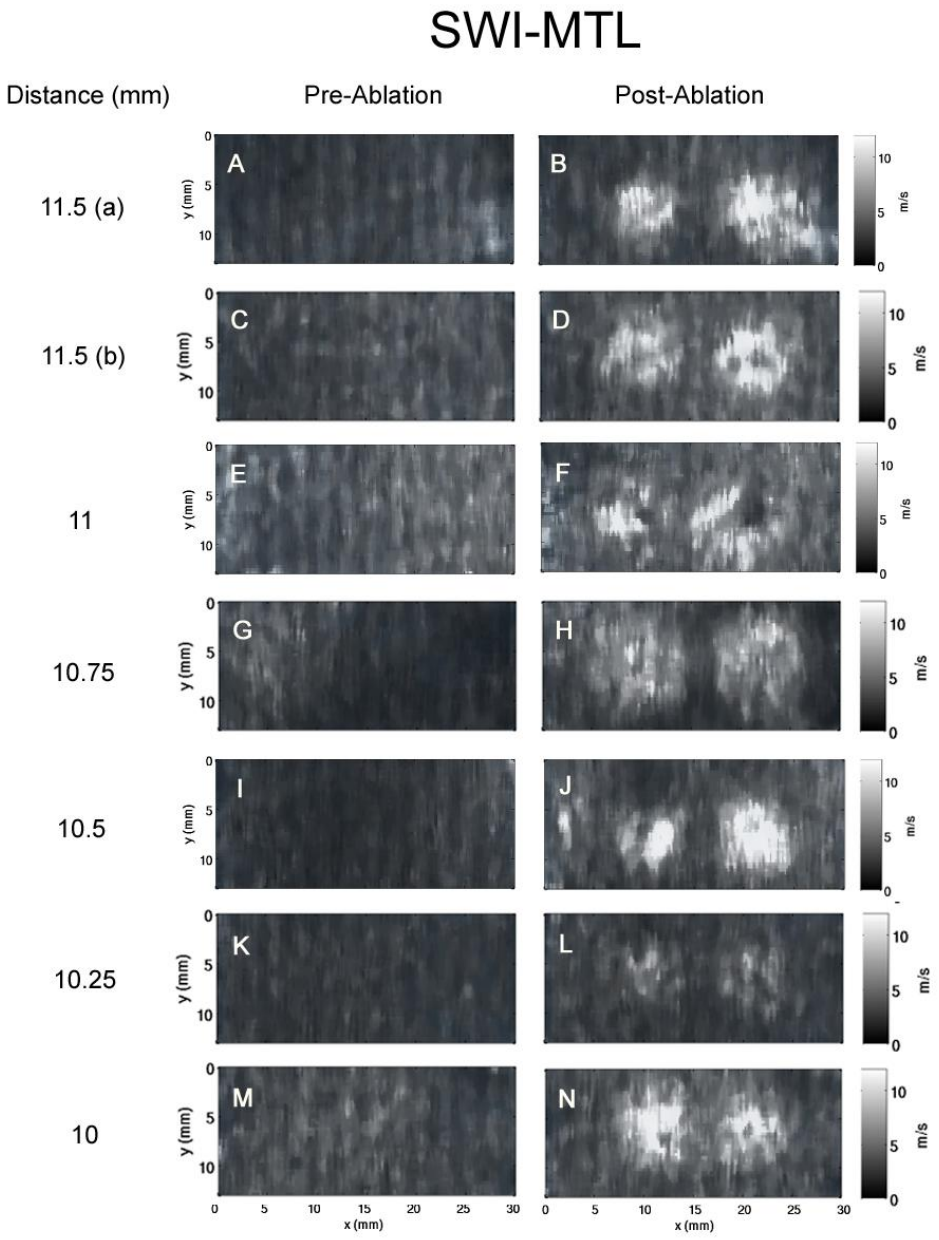

Figure 6: Cross-sectional pre- and post- ablation SWI-MTL scans were constructed from the 3D imaging volume. Distance is measured between lesion centers. Shear wave velocity estimates are shown as a dynamic range between 0 and 10 m/s.

3.1.2.4 Histology (TTC) Stain

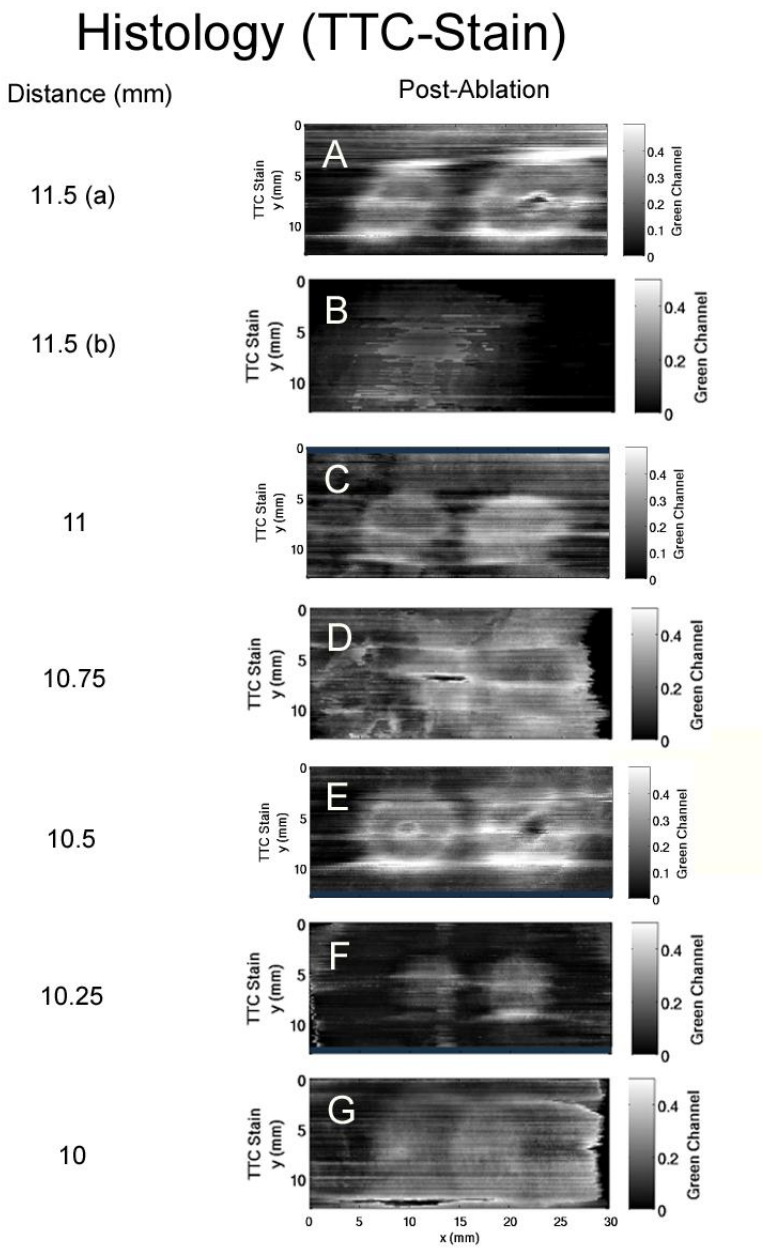

Figure 7: Cross-sectional post-ablation histology (TTC) stain images were constructed from the 3D volume of histology photographs, where imaging slices were taken in the elevational imaging plane. In each case, the axial depth was chosen to correspond to the depth used in the ARFI/SWI result images.

3.1.2.5 Imaging Comparison for Non-Discernible Boundary, Gap Spacing

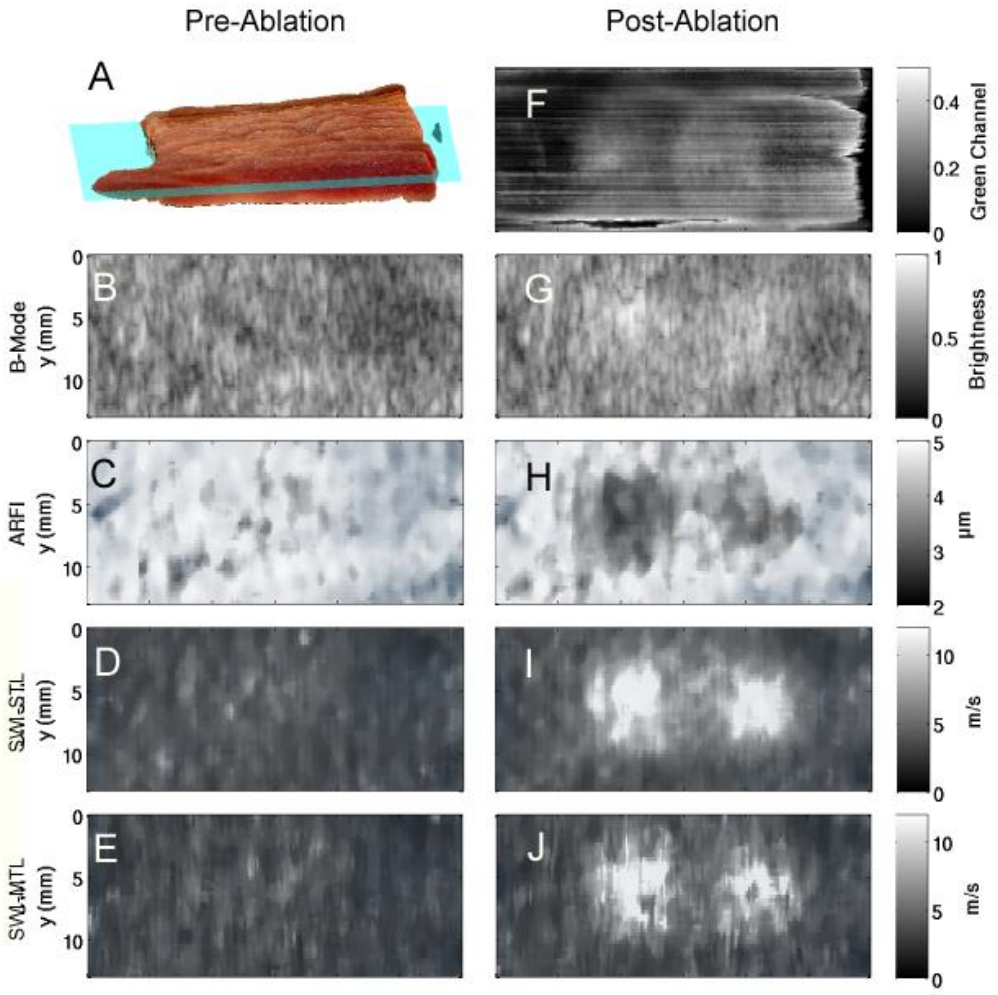

Figure 8: A comparison between all imaging modalities can be seen in this pre- and post-ablation set, where the distance between ablations is 10 mm. Gap spacing in the (F) TTC-stained tissue is indiscernible.

3.1.3 Axial-Lateral Planar Imaging Modality Comparison

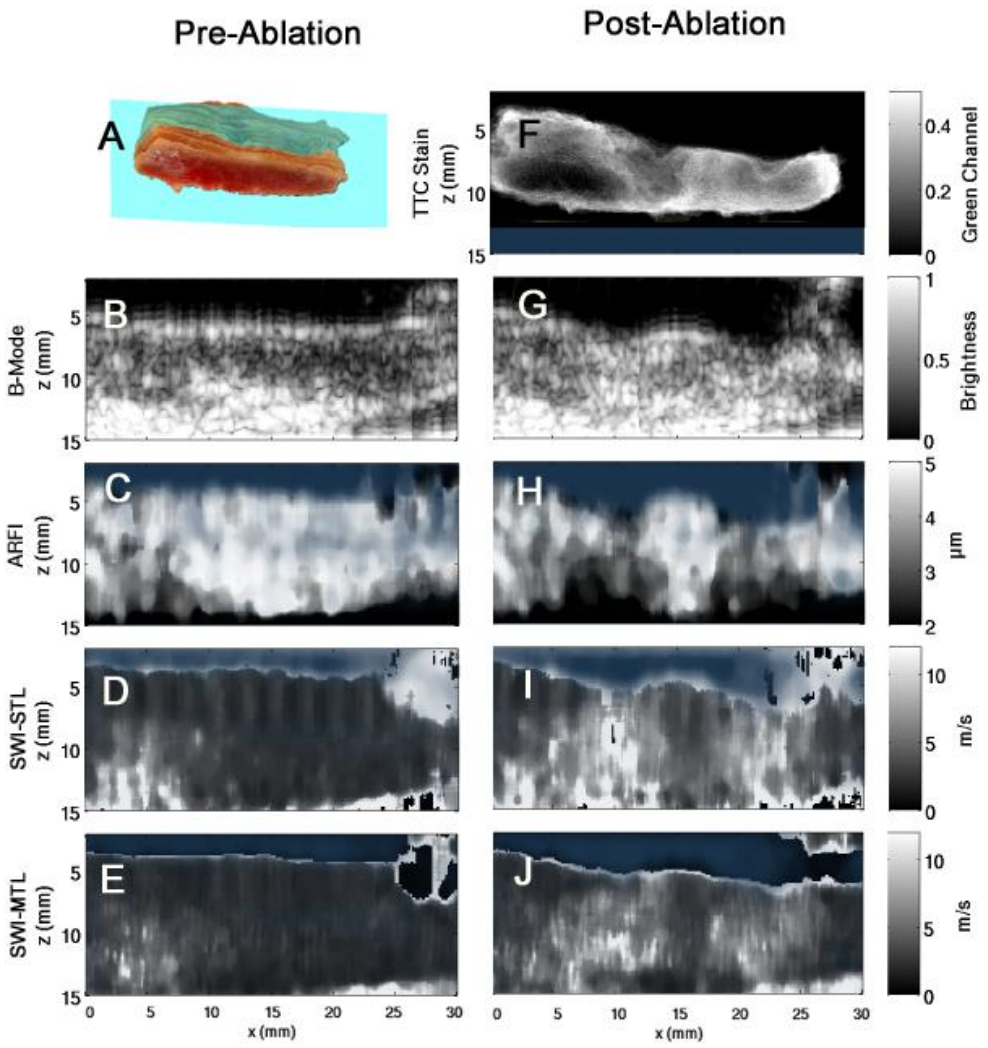

Figure 9: An axial-lateral planar pre- and post- ablation image set was constructed from the 3D data volume through a slice along the approximate center of the ablation lesions. (A): Re-constructed TTC-stain 3D volume showing the axial-lateral plane in relation to the volume. (B) B-Mode pre-ablation; (C) ARFI pre-ablation; (D) SWI-STL pre-ablation; (E) SWI-MTL pre-ablation; (F) TTC-stained cross-section; (G) B-Mode post-ablation; (H) ARFI post-ablation; (I) SWI-STL post-ablation; (J) SWI-MTL post-ablation

3.1.4 Axial-Lateral Planar Gap Variation Comparison

3.1.4.1 ARFI

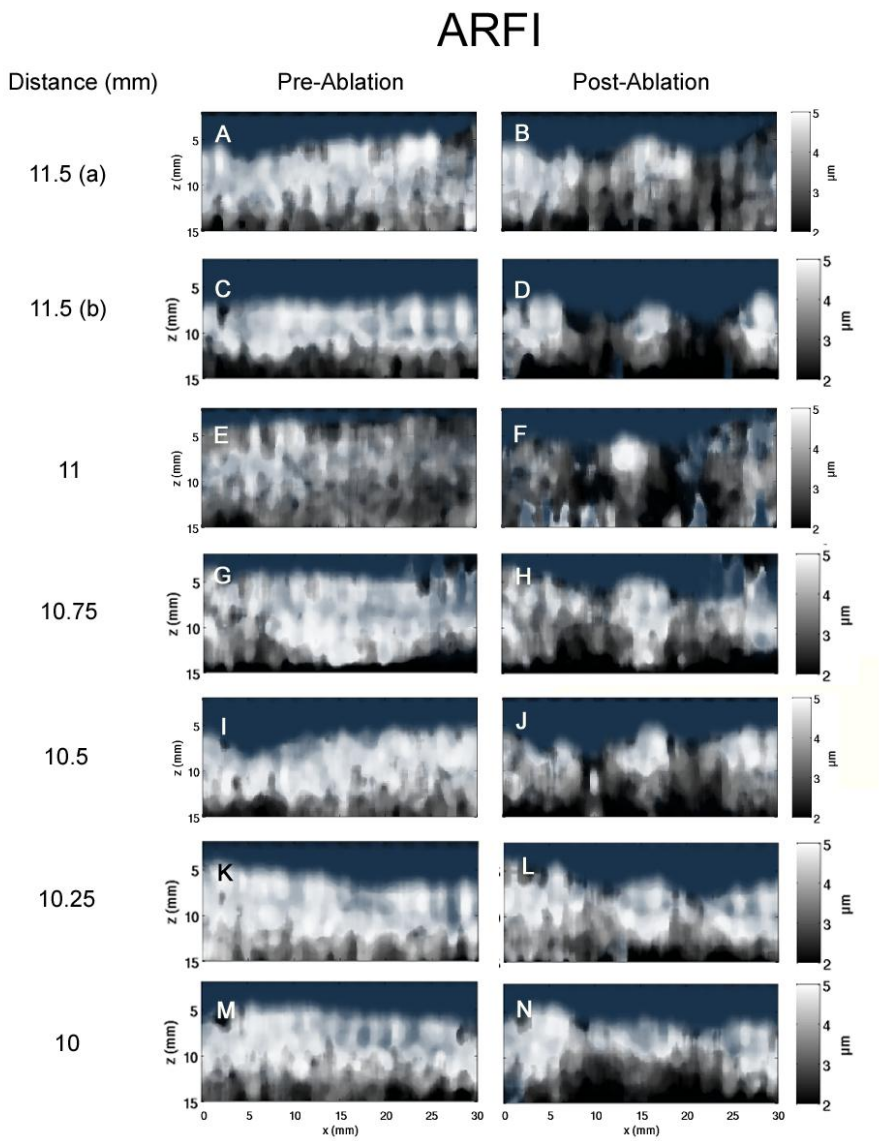

Figure 10: Sets of pre- and post- ablation ARFI images down the center axial-lateral plane of the lesions are shown for each sample. Distance is measured between lesion centers. The measured ARFI displacements are shown as a dynamic range between 2 and 5 μm.

3.1.4.2 SWI-STL

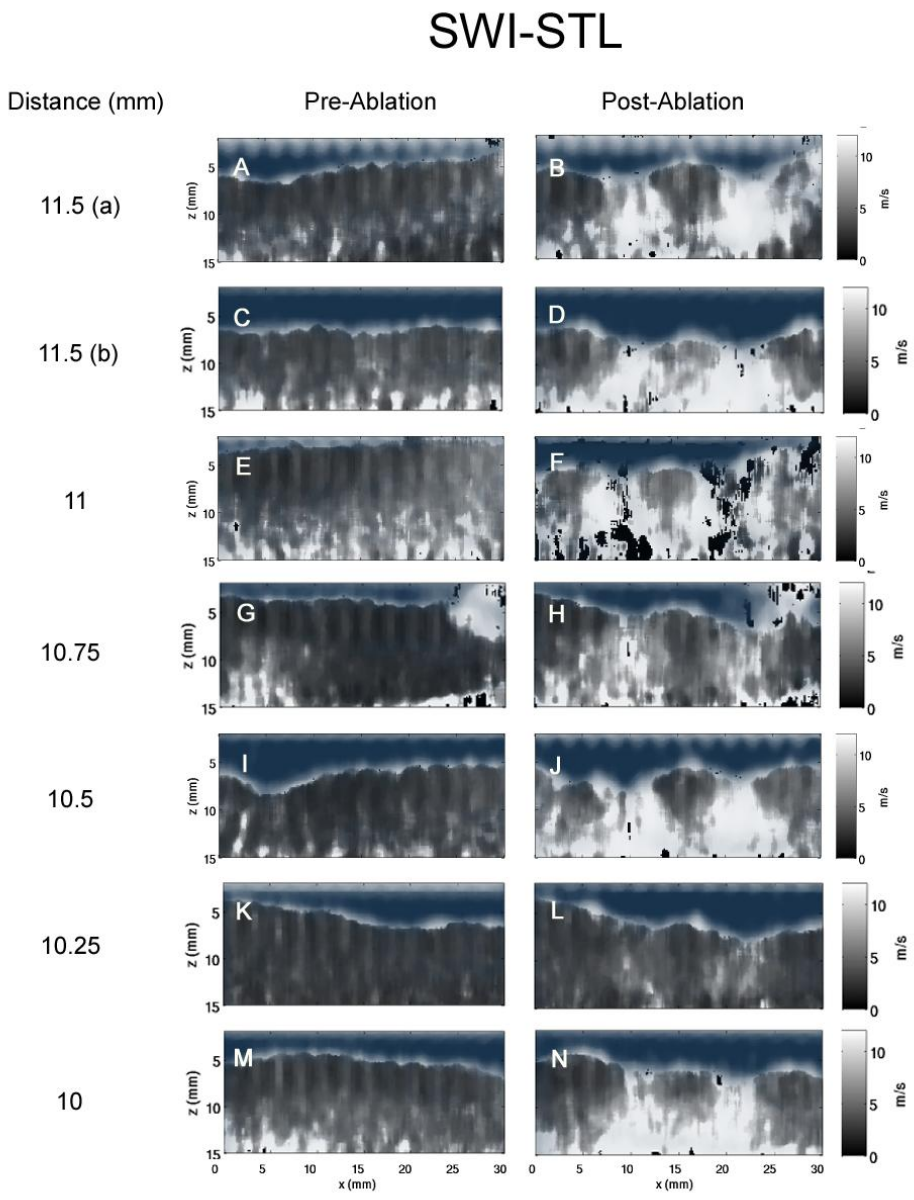

Figure 11: Sets of pre- and post- ablation SWI-STL images down the center axial-lateral plane of the lesions are shown for each sample. Distance is measured between lesion centers. The shear wave velocity estimates are displayed as a dynamic range between 0 and 10 m/s.

3.1.4.3 SWI-MTL

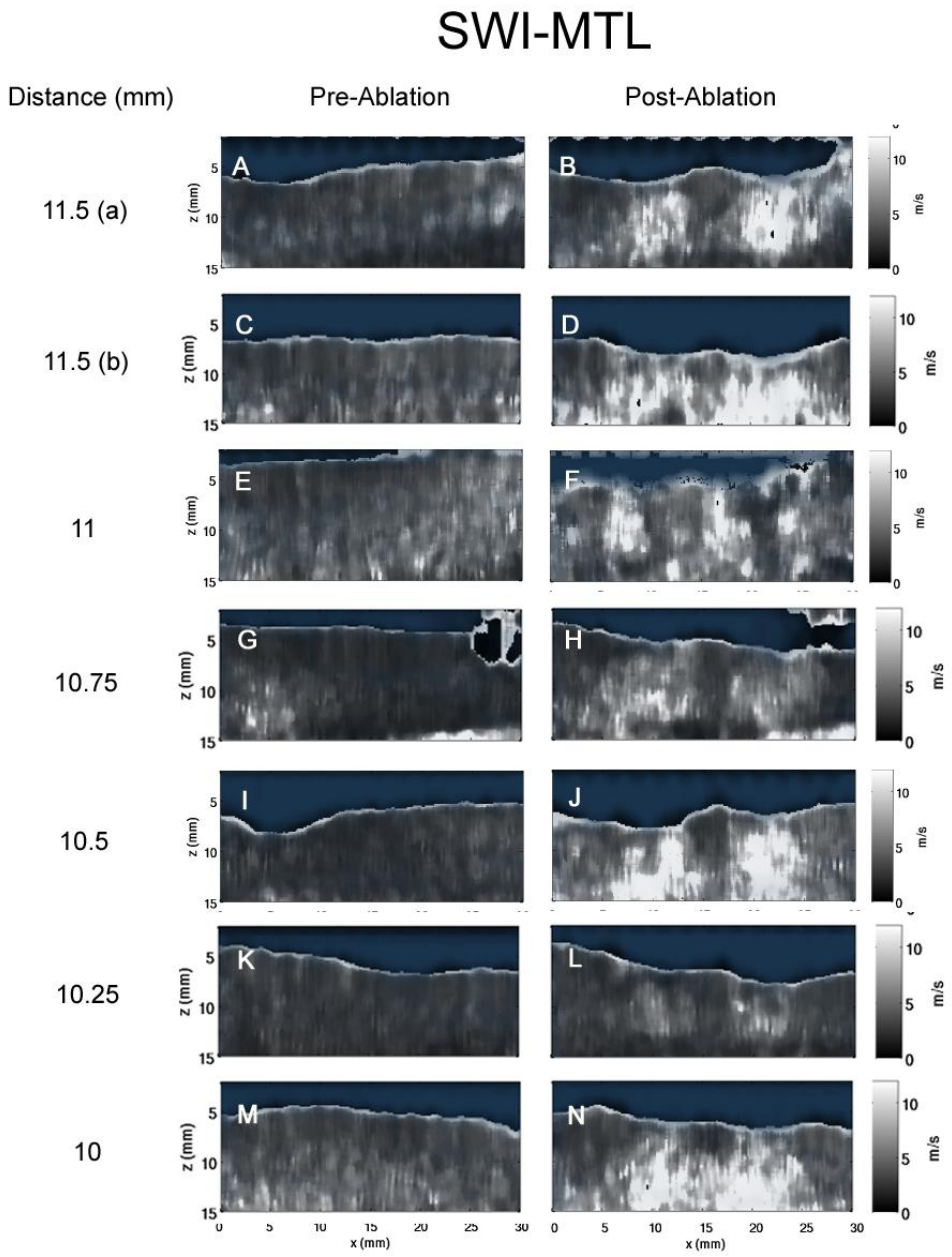

Figure 12: Sets of pre- and post- ablation SWI-MTL images down the center axial-lateral plane of the lesions are shown for each sample. Distance is measured between lesion centers. The shear wave velocity estimates are displayed as a dynamic range between 0 and 10 m/s.

3.1.5 Linear Ablation: Cross-sectional Imaging Modality Comparison

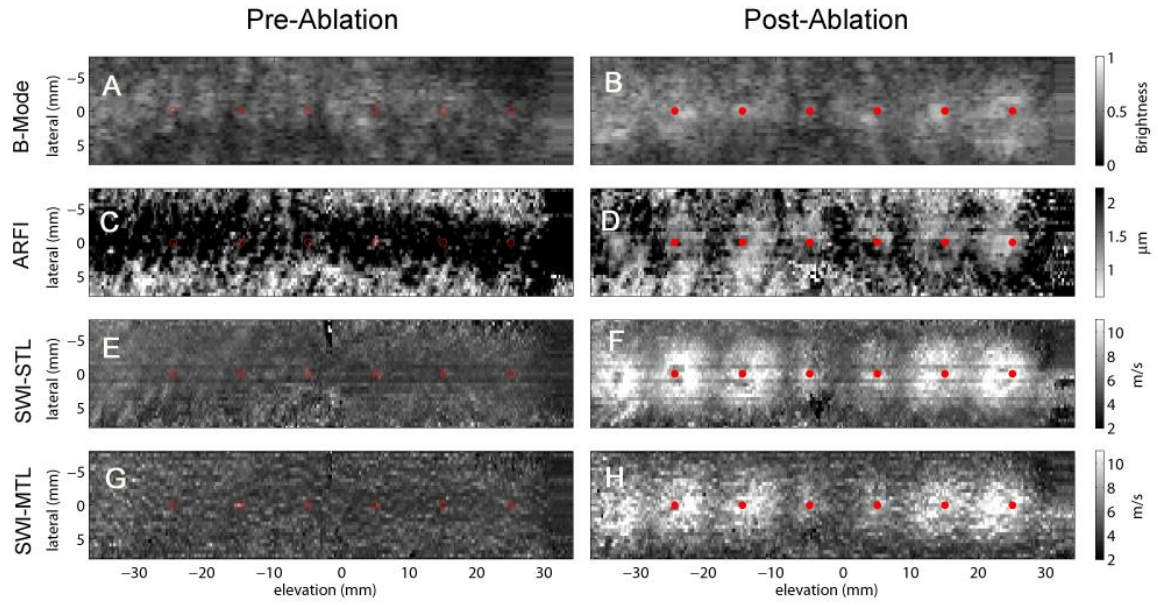

Figure 13: The pre- and post- ablation data was synthesized to show a cross-sectional line of ablation lesions measuring 10 mm apart between lesion centers. The red dots are superimposed on the images at the locations where ablation was performed. (A&B): Pre- and post- ablation cross-sectional B-Mode scans of the entire sample, showing normalized brightness. (C&D): ARFI images where the dynamic range shows ARFI displacement ranging from 0 to 2 µm. (E&F): SWI-STL images where the shear wave velocity estimates range 2 to 10 m/s. (G&H): SWI-MTL images where the shear wave velocity estimates range 2-10 m/s.

3.1.6 Linear Ablation: Gap Variation Comparison

3.1.6.1 ARFI

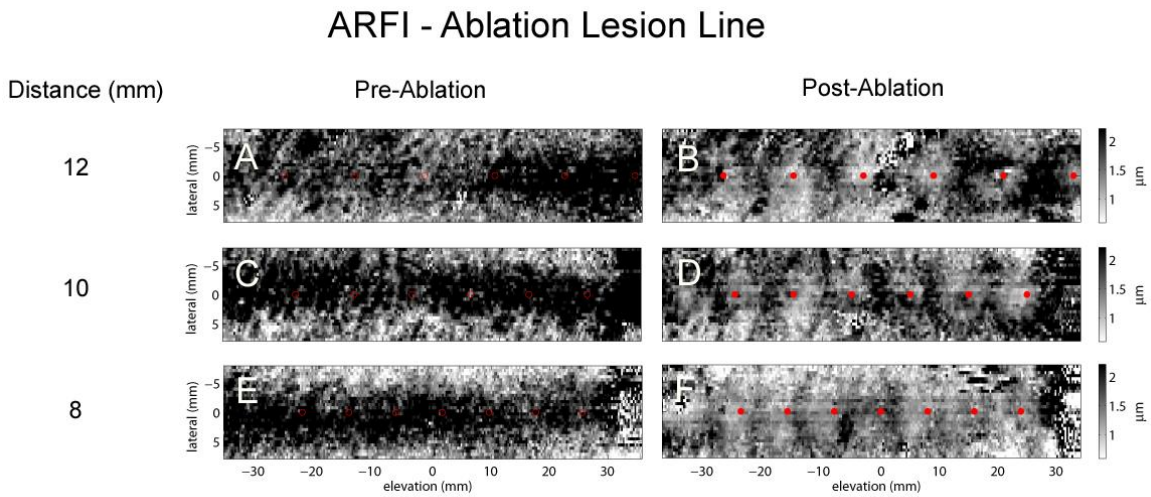

Figure 14: Cross-sectional ARFI images were constructed for pre- and post- ablation data. ARFI displacement ranged from 0 to 2 µm; distances between ablation location ranged 8 to 12 mm. Superimposed red dots appear where ablation was performed.

3.1.6.2 SWI-STL

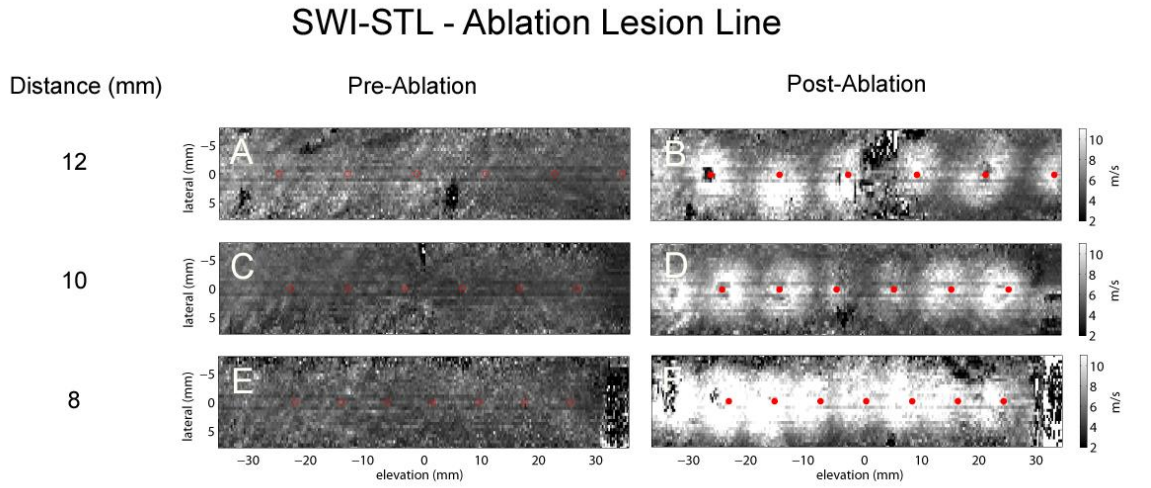

Figure 15: Cross-sectional SWI-STL images were. Shear wave velocity estimates ranged 2-10 m/s. Superimposed red dots appear where ablation was performed.

3.1.6.3 SWI-MTL

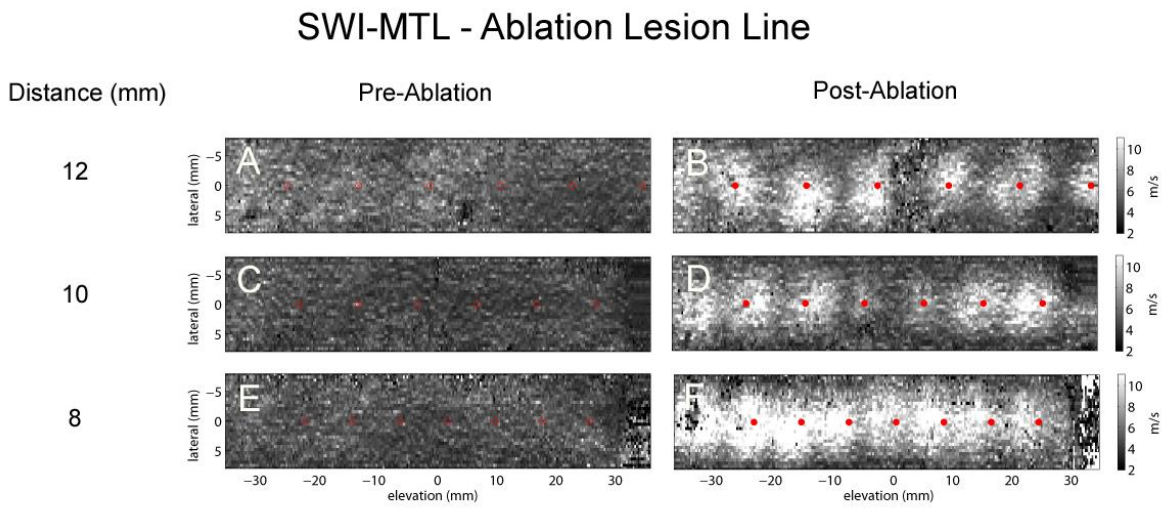

Figure 16: Cross-sectional SWI-MTL images were. Shear wave velocity estimates ranged 2-10 m/s. Superimposed red dots appear where ablation was performed.

3.2 Analysis of methods

3.2.1 Gap Spacing

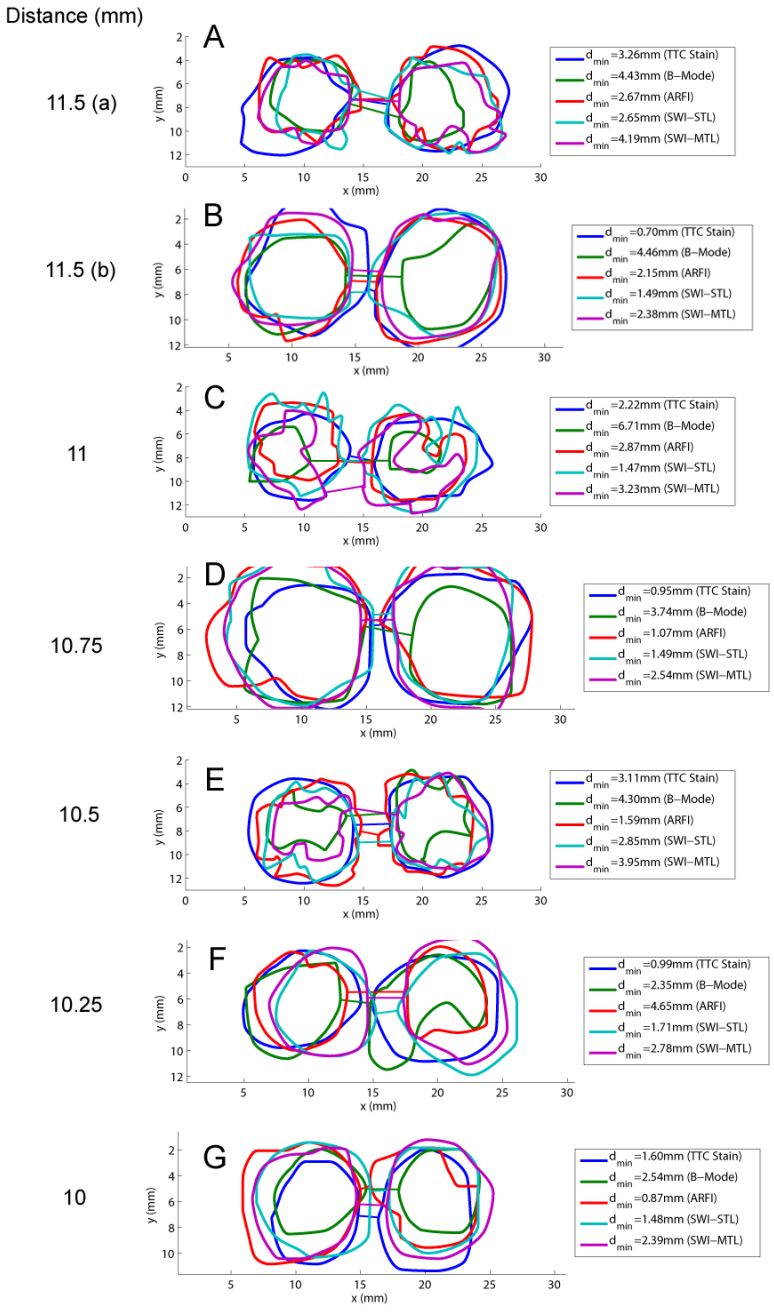

Figure 17: Manually segmented lesions from c-scan images were created for each imaging modality. Gap spacing was measured at closest distance between lesions.

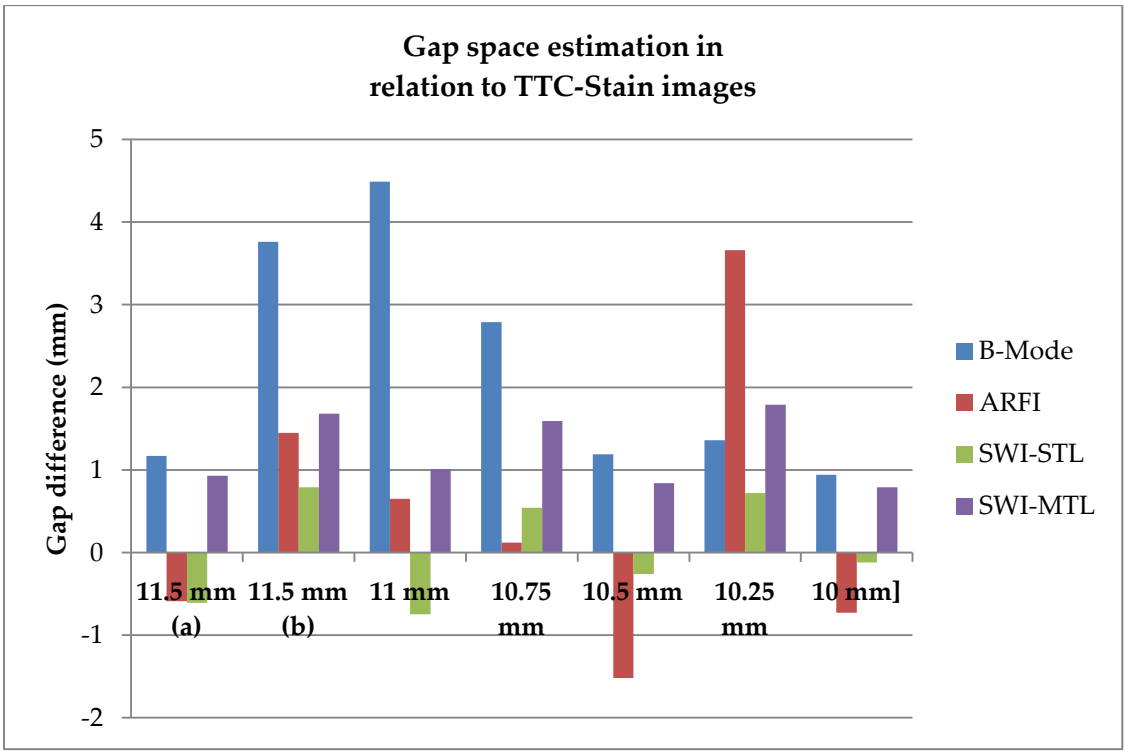

Figure 18: The gap size difference between each imaging modality and the comparable gold-standard TTC-stained c-scan was measured for each sample.

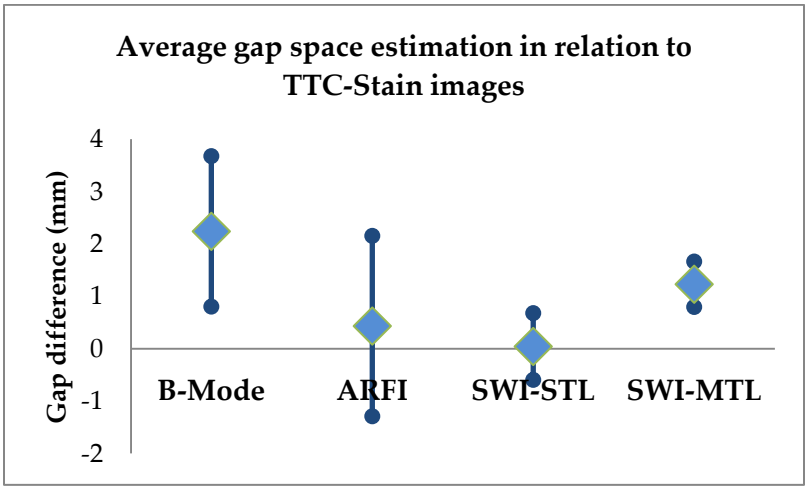

Figure 19: The gap difference between modality and TTC-stain was averaged to demonstrate the over- and under-estimation of gap sizes across modalities. Values that measure closer to 0 have better gap size resolution.

3.2.2 Contrast and Contrast-to-Noise Ratio – Entire Lesion

3.2.2.1 Percent Difference

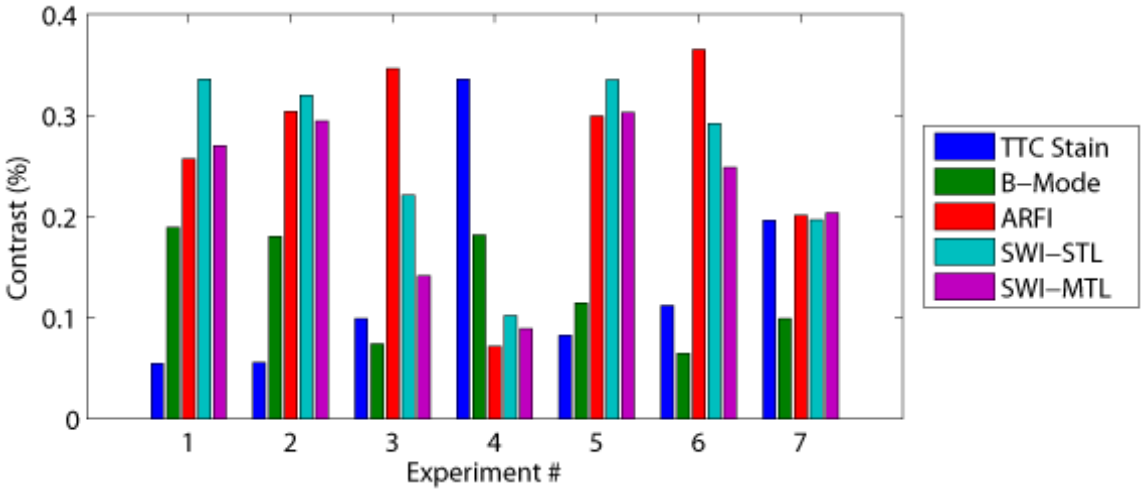

Figure 20: Contrast difference was measured after manual segmentation of the lesions. The experiment numbers refer to samples from different test dates. To reference distance between ablation: (1) 11.5 mm (a), (2) 10.5 mm, (3) 11 mm, (4) 10.25 mm, (5) 10 mm, (6) 11.5 (b), and (7) 10.75 mm.

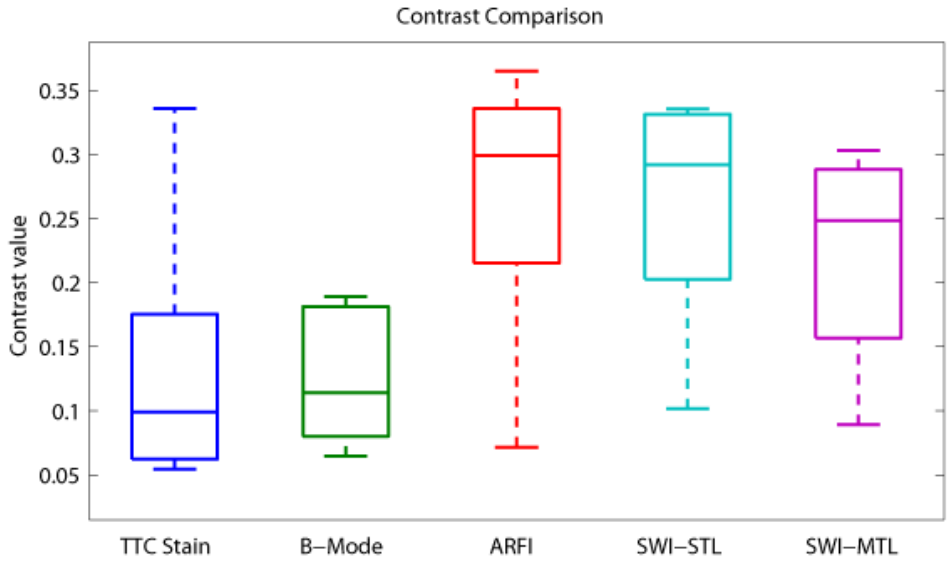

Figure 21: Contrast difference was averaged across the samples and compared with values across different imaging modalities.

3.2.2.2 Contrast-to-Noise Ratio

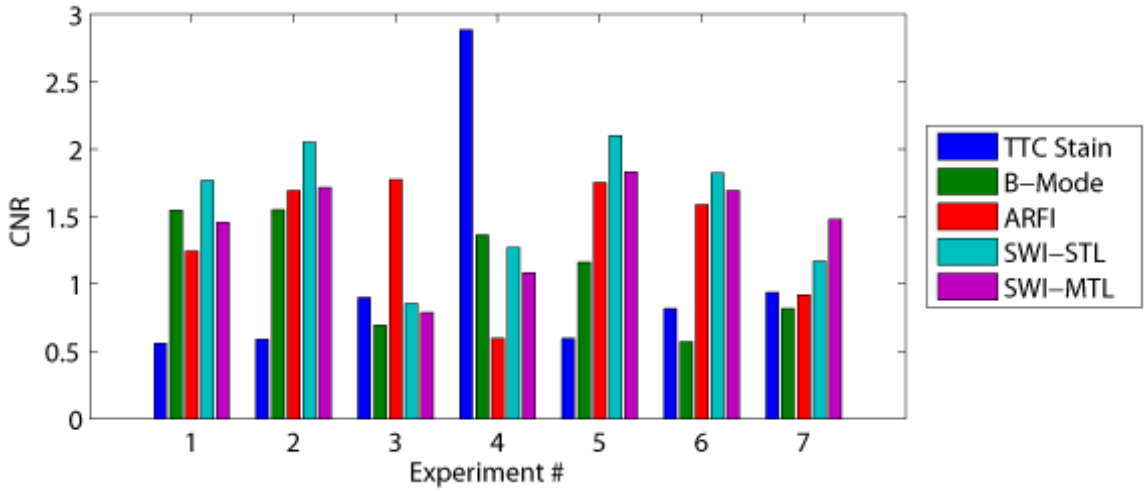

Figure 22: Contrast-to-noise ratio (CNR) was measured after manual segmentation of the lesions. The experiment numbers refer to samples from different test dates. To reference distance between ablation: (1) 11.5 mm (a), (2) 10.5 mm, (3) 11 mm, (4) 10.25 mm, (5) 10 mm, (6) 11.5 (b), and (7) 10.75 mm.

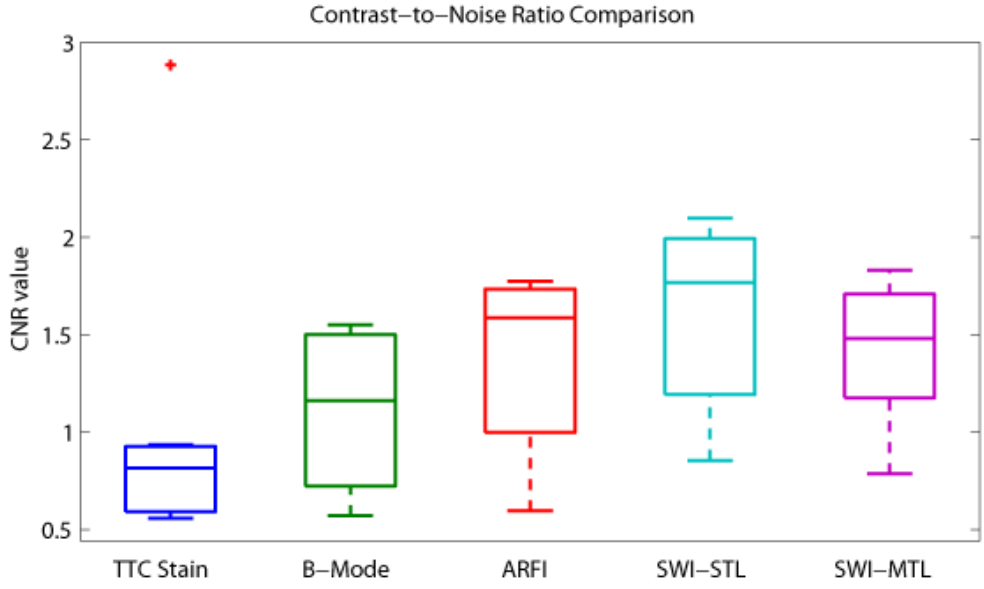

Figure 23: CNR values were averaged across the samples and compared with average CNR values across different imaging modalities.

3.2.3 Contrast and Contrast-to-Noise Ratio – 1/3 Lesion

3.2.3.1 Percent Contrast

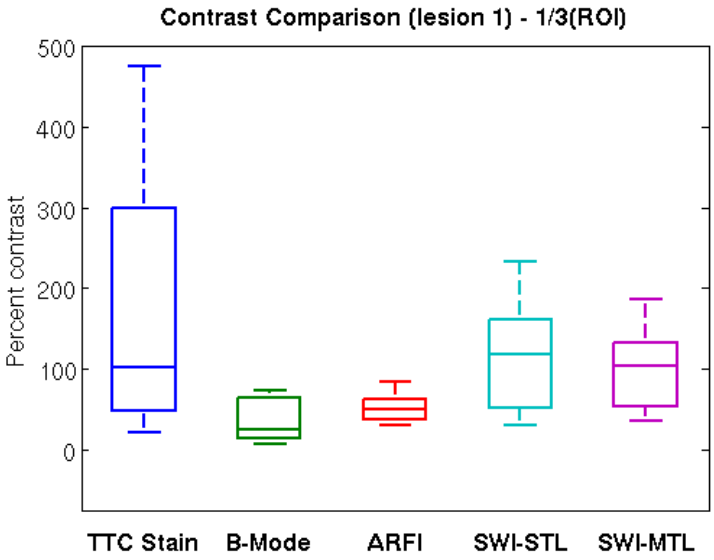

Figure 24: Percentage contrast for a one-third area defined region within the segmented lesion 1 was calculated.

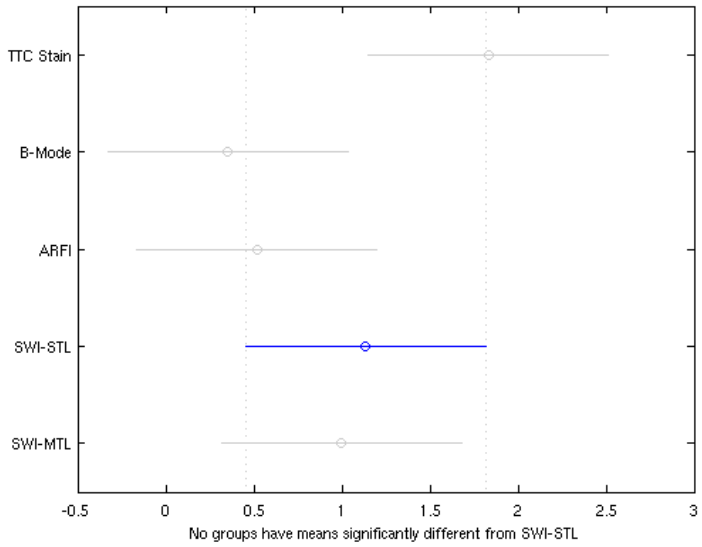

Figure 25: The one-way analysis of variance (ANOVA) statistical test was used to compare the percent contrast values for lesion 1.

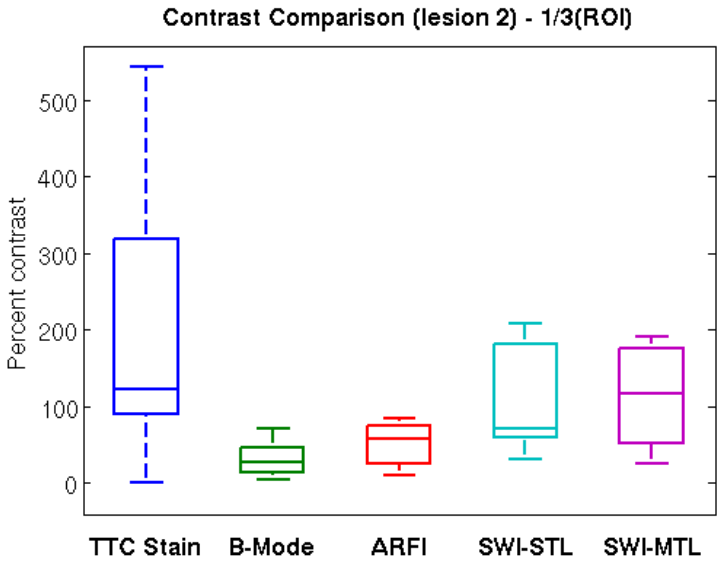

Figure 26: Percentage contrast for a one-third area defined region within the segmented lesion 2 was calculated.

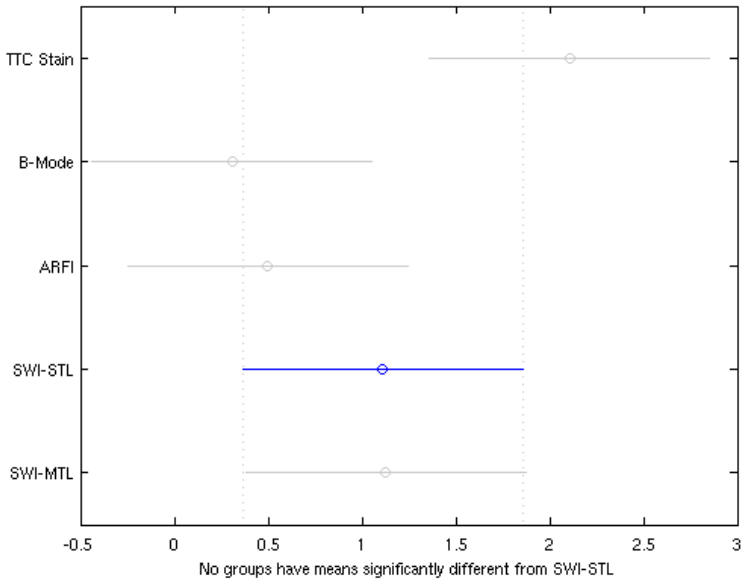

Figure 27: The one-way analysis of variance (ANOVA) statistical test was used to compare the percent contrast values for lesion 2.

3.2.3.2 Contrast-to-Noise Ratio

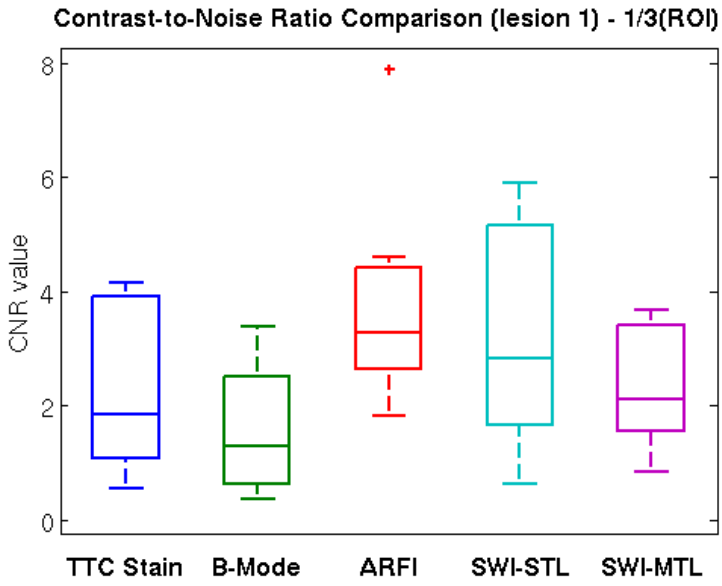

Figure 28: CNR for a one-third area defined region within the segmented lesion 1 was calculated.

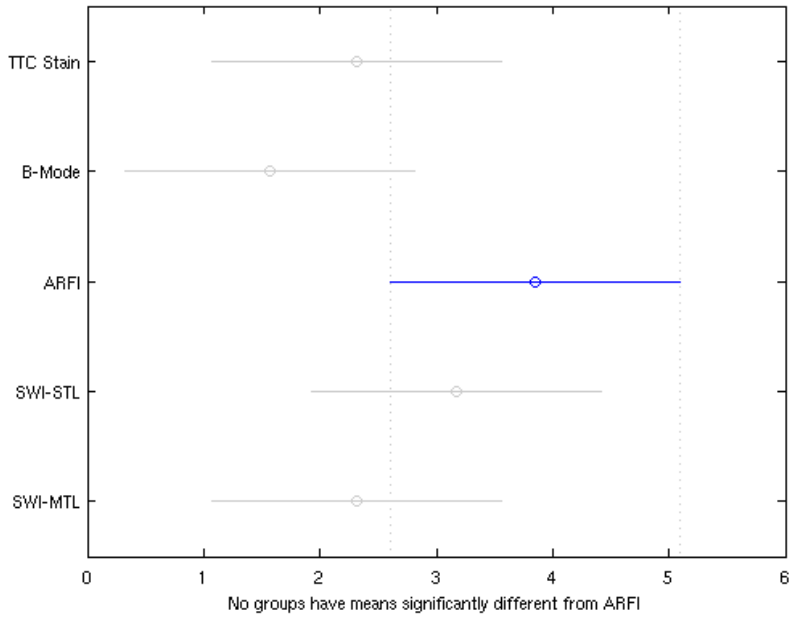

Figure 29: The ANOVA statistical test was used to compare the CNR values for lesion 1.

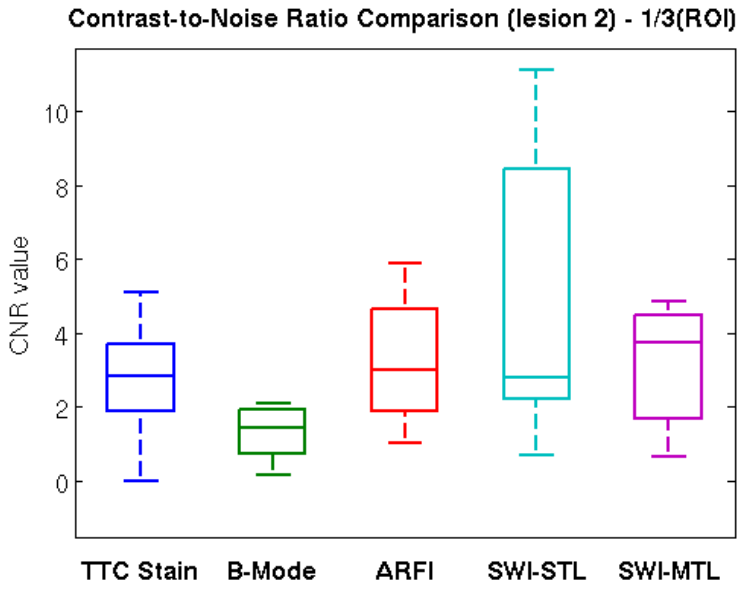

Figure 30: CNR for a one-third area defined region within the segmented lesion 1 was calculated.

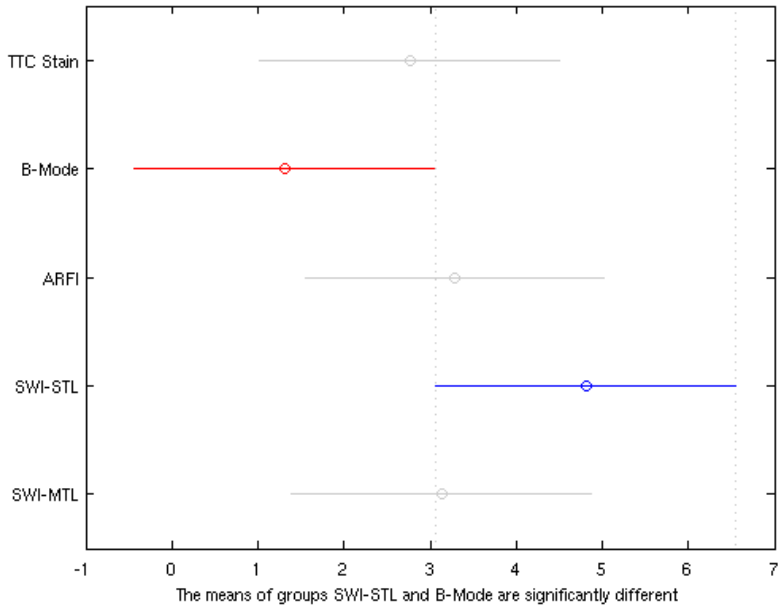

Figure 31: The ANOVA statistical test was used to compare the CNR values for lesion 2.

3.2.3.3 Contrast Difference

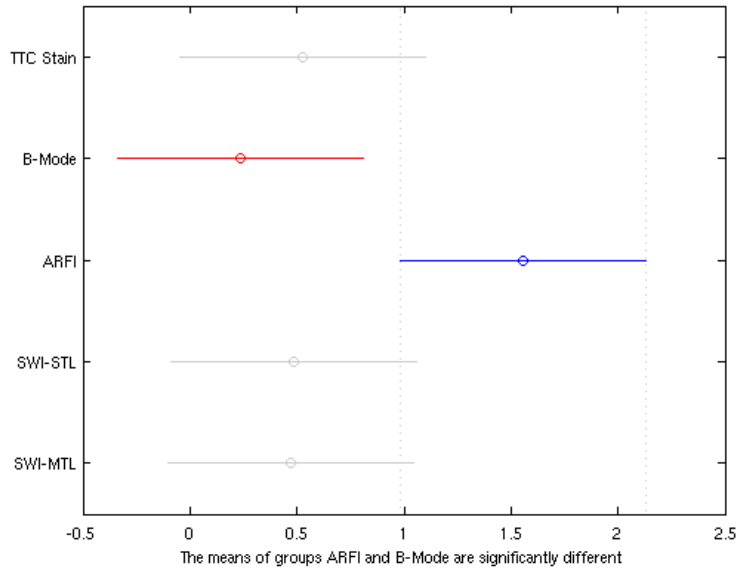

Figure 32: ANOVA for contrast difference between inside 1/3 of the lesion and outside the lesion was calculated for Lesion 1.

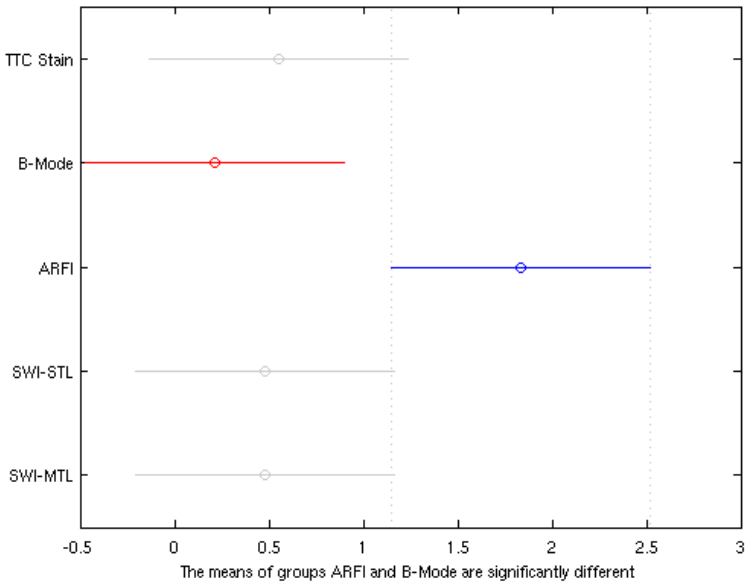

Figure 33: ANOVA for contrast difference between inside 1/3 of the lesion and outside the lesion was calculated for Lesion 2.

4. Discussion

4.1 Ablation Lesion Imaging

In each sample of the ablation pair experiments, both cross-sectional scan images and axial-lateral planar images were synthesized to compare axial, lateral, and elevational resolution in ARFI and SWI images. In both ARFI and SWI data acquisition, the same ARFI excitation and time-to-peak displacement tracking sequences were used.

4.1.1 Cross-sectional Imaging Modality Comparison

The side-by-side comparison of images generated from each modality in both pre-ablation and post-ablation states demonstrates viability for visualization and identification of a pair of lesions and the gap spacing between lesions. Increased echogenecity of the post-ablation B-Mode image (Figure 3(G)) is unexpected. It has been reported that RF lesions are hypoechoic following treatment in some patients; this explanation may hold true in this experimental set-up.[1]

Myocardial structures are visible in the pre-ablation images. While the tissue samples were chosen for endocardial surface smoothness, underlying muscular structures (papillary muscles originating under the endocardium) were not accounted for. Because RFA lesion growth relies on thermal conduction, muscular structures may have influenced the thermal conduction pathway and resulting lesion growth. In the RFA treatment of ventricular fibrillation, it has been shown that ablation in the vicinity

[1] (Lorentzen, et al. 1997)

of papillary muscles have affected the transmurality and linear ablation completeness of RFA lesions.[2]

The cross-sectional scan (c-scan) depth of each imaging modality (B-Mode, ARFI, SWI-STL, and SWI-MTL) is highly comparable because the data from which images were synthesized is over the same 3D volume, with no variation in overall size or position. The 3D volume of tissue histology is synthesized from images taken of the tissue sample after freezing, slicing, staining, embedding and freezing, and cryoslicing. While the geometry of the tissue sample was kept as close to imaging geometry as possible, slight deformation of the tissue volume was inevitable. Deformation could have been caused by tissue dehydration or embedding, where bent corners or crinkled epicardial surfaces of the sliced tissue would have slightly altered the geometric configuration of the tissue. The histology c-scan (Figure 3(F)) was chosen at a depth that most closely matched to the imaging depth slice of the imaging data set based on measurement from the endocardial surface. The most accurate mode of comparison would be a 3D imaging volume overlaid on the 3D reconstructed histology for lesion boundary and gap size measurement comparison.

4.1.2 Cross-sectional Gap Variation Comparison

Because a point of interest in this study was to understand the ability of ARFI/SWI in resolving lesions and their small ($\leq 2\ mm$) gap spacing, the distance

[2] (Pak, et al. 2006)

between lesions was varied from 11.5 mm and incremental decreases in each sample to 10 mm ablation distance. The ARFI, SWI-STL, and SWI-MTL pre- and post- ablation image sets show the variability in lesion size and gap size even with RFA procedural controls, such as power delivery, catheter tip irrigation, temperature of surrounding fluid, and duration of RF delivery. Across figures 4, 5, and 6, we are able to show how inherent myocardial structures affect lesion growth. In pre-ablation figures 4(G), 5(G), and 6(G), a relatively stiff underlying structure is visible on the upper left corner of the c-scan. The structure appears to affect the lesion boundary in figures 4(H), 5(H), and 6(H). Using current ablation assessment methods like EAM, this extended lesion boundary would not have been identified, and in linear ablation, could have resulted in unexpected necrosis discontinuity.

As the distance between ablation decreases, the gap size appears smaller as expected (Figures 4(N), 5(N), and 6(N)). However, the boundaries between the lesions become less clear, and the histology c-scan does not show a clear gap between the pair of lesions, as in Figure 6(F). Gaps measuring less than 1 mm were not achieved with decreasing ablation distance; a possible explanation for this behavior may relate to thermal conduction in the tissue. Lesions were created with clinically relevant timing in mind – time between subsequent ablations was less than 2 minutes. During this time, the tissue may not have had time to cool to physiologic temperature, and thermal conduction would have easily crossed into recently ablated tissue.

4.1.3 Linear ablation: Cross-sectional Imaging and Gap Variation

To demonstrate the robustness of ARFI/SWI in a more clinically relevant experiment, the line of lesions were imaged using the clinical ARFI/SWI sequence. The distance between ablations ranged from 8 mm to 12 mm, for a total of three different tissue samples. A distance of 8 mm was chosen because we had hypothesized that 8 mm spacing between ablations would result in lesion overlap and no conduction gaps between lesions through the center elevational axis. This lesion boundary overlap can be seen clearly in Figures 15(F) and 16(F), the SWI-STL and SWI-MTL images, respectively. On the other hand, the ARFI image in Figure 14(F) shows identifiable gaps, although the lesion boundaries appear unclear. That ARFI was able to show gap spacing between lesions while SWI modalities were not able to show spacing is very clinically relevant; this is particularly important because the cross-sectional scan was synthesized from the same imaging data set at the same depth across all modalities.

Lesion placement was controlled for by the precise motion of the translational stage used during experimentation, and yet the lesion centers do not appear to always fall at the pre-determined ablation location. This significance should be noted because even with an *ex-vivo* experiment with highly controlled ablation conditions (power, duration, best estimation of tip contact, temperature), lesions varied greatly in size. Endocardial surface variation due to muscle striations and valvular and venous structures make uniform ablation tip contact very difficult. Between muscle striations,

ablation catheters are prone to dipping further into the tissue than the expected surface; thermal conductivity is more potent in ablation between structures. In cross-sectional and axial-lateral planar images, these structures are not identifiable. Reconstructed three-dimensional imaging data is useful in such structural anatomy identification; this added structural information can help specialists to prepare for non-uniform lesion formation during radiofrequency ablation procedures.

4.2 Accuracy of Modalities

4.2.1 Gap Size Estimation

After manual segmentation of the lesions, the smallest gap between lesions was measured and compared with that of the histology (TTC-stain) images. The figures generated by the segmentation show highly varying gap sizes. Unexpectedly, the gap size measured with TTC-stain images did not follow a linear relationship with the ablation distance. Though axial depth was chosen to reflect the myocardial c-scan at the focal depth, the TTC-stain images used for point-of-comparison were not perfectly aligned.

The current c-scan and segmentation method does not utilize 3D volume rendering and re-slicing. Superimposing the entire three-dimensional volume of an ARFI/SWI data set onto the histology volume would provide complete size and gap matching. The 2D segmentation method presupposes that the axial slice through the 3D

data set is always along the same axis of rotation, which is not necessarily an accurate representation of the axial slice through the volumetric histology data.

Overall, gap size estimation is best predicted by SWI-STL, followed by ARFI imaging. The estimation accuracy assumes that the histology data is a true gold standard, and does not account for TTC-stain inaccuracies. There may be a source of error in the stain data because TTC stain was found to bleed into the embedding OCT medium slightly. Therefore, at the endocardial surface, the contrast between surrounding tissue and lesion is not entirely clear.

4.2.2 Contrast-to-Noise Ratio, Percent Contrast

To define the regions of interest in contrast-to-noise ratio (CNR) and percent contrast calculations, the centroid of the overall segmented lesions were found. A circular area defined around the centroid equal to one-third of the original TTC-stained lesion size, and the mean and standard deviation of the data was found inside the defined areas of each lesion, across each modality. A region with the same defined area was chosen outside the segmented lesions in the TTC-stained image to calculate the mean and standard deviation of each set of modality data outside the lesions. These values were used to calculate the CNR and percent contrast.

These CNR and percent contrast values were then analyzed using a one-way Analysis of Variance (ANOVA) statistical test to demonstrate the differences across the resolution of the different modalities. The TTC-stain, B-Mode, ARFI, SWI-STL, and SWI-

MTL data were analyzed and compared with each other. The multiple-compare results of the ANOVA statistical test can be seen in Figures 25, 27, 29, and 31.

Calculated CNR values in ARFI, SWI-STL, and SWI-MTL differ from the values calculated in the B-Mode images. In the CNR calculation for Lesion 2, SWI-STL demonstrated significantly different CNR values from B-Mode across the experiments. As the B-Mode data provides physical information about the differences in tissue echogenicity, the lesions are not expected to have significant contrast with the area outside the lesions. Except in cases of hypoechoic lesions, the B-Mode images are not expected to show high CNR or percent contrast.

The calculated percent contrast values in ARFI, SWI-STL, and SWI-MTL did not show significant difference from the values calculated in B-Mode images. The contrast differences across modalities were calculated as a difference between the mean values inside and outside the region of interest within the defined lesion. In the analysis of contrast difference, ARFI demonstrated a significantly different value than the contrast difference value of B-Mode data. This difference can be seen upon visual inspection of the c-scan results, and may be explained by the small dynamic range of the ARFI data, which was ranged across 2-5 μm displacement.

5. Conclusion

ARFI and shear wave-based methods (SWI-STL and SWI-MTL) were used to image pairs and lines of RFA lesions in *ex vivo* porcine ventricular tissue. Overall, SWI-STL and ARFI data processing yielded the best results in identification of lesion boundaries and gap spacing. Both ARFI and SWI-methods appear to be viable methods of identifying gaps between ablation lesions.

Differences in resolution across the modalities (ARFI, SWI-STL, and SWI-MTL) are not significant. Based on this conclusion, each of these elasticity imaging modalities are viable methods of identifying myocardial ablation lesions in a controlled, *ex vivo* setting. In further understanding the differences in resolving ability of each of the elasticity imaging modalities, it is important to apply these methods in *in vivo* experiments, where the bulk motion of the tissue may affect the calculation of the shear wave velocities and ARFI displacements. In such cases, it will be important to test the differences between the SWI-STL and SWI-MTL methods, which utilize different shear wave velocity measurements based on spatially modulated and multiple-track averaged ultrasonic track locations.

References

Dewire, Jane, and Hugh Calkins. "State-of-the-art and emerging technolgies for atrial fibrillation ablation." *Nature Reviews*, 2010: 129-138.

Dubin, Dale. *Rapid Interpretation of EKG's.* Tampa: COVER Publishing Company, 2000.

Eyerly, Stephanie A., et al. "Intracardiac acoustic radiation force impulse imaging: A novel imaging method for intraprocedural evaluation of radiofrequency ablation lesions." *Heart Rhythm Society*, 2012: 1855-1862.

Fahey, Brian J., Kathryn R. Nightingale, Stephen A. McAleavey, Mark L. Palmeri, Patrick D. Wolf, and Gregg E. Trahey. "Acoustic Radiation Force Impulse Imaging of Myocardial Radiofrequency Ablation: Initial In Vivo Results." *IEEE Transactions on Ultrasonics, Ferroelectrics, and Frequency Control*, 2005: 631-641.

Fishbein, et al. "Early phase acute myocardial infarct size quantification: Validation of the triphenyl tetrazolium chloride tissue enzyme staining technique." *American Heart Journal*, 1981: 593-600.

Ho, Siew Yen, Damian Sanchez-Quintana, Jose Angel Cabrera, and Robert H. Anderson. "Anatomy of the Left Atrium: Implications for Radiofrequency Ablation of Atrial Fibrillation." *Journal of Cardiovascular Electrophysiology*, 2007: 1525-1533.

Jain, Mudit K., and Patrick D. Wolf. "Temperature-controlled and constant-power radio-frequency ablation: what affects lesion growth?" *IEEE Transactions on Biomedical Engineering*, 1999: 1405-1412.

Kastor, John A. *Arrythmias.* Philadelphia: W. B. Saunders Company, 2000.

Lorentzen, Torben, Niels Erik Holm Christensen, Christian P. Nolsoe, and Soren T. Torp-Pedersen. "Radiofrequency Tissue Ablation with a Cooled Needle in Vitro: Ultrasonography, Dose Response, and Lesion Temperature." *Academic Radiology*, 1997: 292-297.

Marrouche, Nassir F., et al. "Phased-Array Intracardiac Echocardiography Monitoring During Pulmonary Vein Isolation in Patients With Atrial Fibrillation: Impact on Outcome and Complications." *Circulation*, 2003: 2710-2716.

McAleavey, Stephen A., Manoj Menon, and Jarrod Orszulak. "Shear-Modulus Estimation by Application of Spatially-Modulated Impulsive Acoustic Radiation Force." *Ultrason. Imag.*, 2007: 87-104.

Melby, Spencer J., et al. "Atrial fibrillation propagates through gaps in ablation lines: Implications for ablative treatment of atrial fibrillation." *Heart Rhythm Society*, 2008: 1296-1301.

Naccarelli, Gerald, Joseph T. Dell'Orfano, Deborah L. Wolbrette, Hemantkumar M. Patel, and Jerry C. Luck. "Cost-effective management of acute atrial fibrillation: role of rate control, spontaneous conversion, medical and direct current cardioversion, transesophageal echocardiography, and antiembolic therapy." *The American Journal of Cardiology*, 2000: 36-45.

Nademanee, Koonlawee, Evan Lockwood, Naoya Oketani, and Brett Gidney. "Catheter ablation of atrial fibrillation guided by complex fractionated atrial electrogram mapping of atrial fibrillation substrate." *Journal of Cardiology*, 2010: 1-12.

Nightingale, Kathryn, Mary Scott Soo, Roger Nightingale, and Gregg Trahey. "Acoustic Radiation Force Impulse Imaging: In Vivo Demonstration of Clinical Feasibility." *Ultrasound in Med. & Biol.*, 2002: 227-235.

Nightingale, Kathryn, Stephen McAleavey, and Gregg Trahey. "Shear-Wave Generation Using Acoustic Radiation Force: In Vivo and Ex Vivo Results." *Ultrasound in Med. & Biol.*, 2003: 1715-1723.

Pak, Hui-Nam, et al. "Role of the Posterior Papillary Muscle and Purkinje Potentials in the Mechanism of Ventricular Fibrillation in Open Chest Dogs and Swine: Effects of Catheter Ablation." *Journal of Cardiovascular Electrophysiology*, 2006: 777-783.

Palmeri, Mark L., and Kathryn R. Nightingale. "Acoustic radiation force-based elasticity imaging methods." *Interface Focus*, 2011: 553-564.

Pappone, Carlo, et al. "Atrial Electroanatomic Remodeling After Circumferential Radiofrequency Pulmonary Vein Ablation: Efficacy of an Anatomic Approach in a Large Cohort of Patients With Atrial Fibrillation." *Circulation*, 2001: 2539-2544.

Sarvazyan, Armen P., Oleg V. Rudenko, Scott D. Swanson, J. Brian Fowlkes, and Stanislav Y. Emelianov. "Shear Wave Elasticity Imaging: A new ultrasonic technology of medical diagnostics." *Ultrasound in Med. & Biol.*, 1998: 1419-1435.

Van Gelder, Isabelle C., Harry J. Crijns, Wiek H. Van Gilst, Remco Verwer, and Kong Lie. "Prediction of Uneventful Cardioversion and Maintenence of Sinus Rhythm from Direct-Current Electrical Cardioversion of Chronic Atrial Fibrillation and aFlutter." *The American Journal of Cardiology*, 1991: 41-46.

Wells, Peter N. T., and Hai-Dong Liang. "Medical ultrasound: imaging of soft tissue strain and elasticity." *Journal of The Royal Society Interface*, 2011: 1521-1549.

Wilber, David J., Douglas L. Packer, and William G. Stevenson. *Catheter Ablation of Cardiac Arrhythmias: Basic Concepts and Clinical Applications.* New York: Blackwell Publishing, 2008.